An Investigation of the Mechanics of an Actin Spring

by

Barney Kwun-poo Tam

Submitted to the Department of Physics
in partial fulfillment of the requirements for the degree of
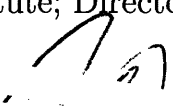
Doctorate of Philosophy in Physics

at the

MASSACHUSETTS INSTITUTE OF TECHNOLOGY

September 2007

© Massachusetts Institute of Technology 2007. All rights reserved.

Author ... .
(/ Department of Physics
July 30, 2007

Certified by... ....
Paul Matsudaira
Professor, Depts. of Biology & Biological Engineering; Member,
Whitehead Institute; Director, MIT/Whitehead Institute BioImaging
Center
Thesis Supervisor

Certified by... ....
Alexander van Oudenaarden
Associate Professor, Dept. of Physics
Thesis Supervisor

Accepted by ....
Thomas Greytak
Chairman, Department of Physics
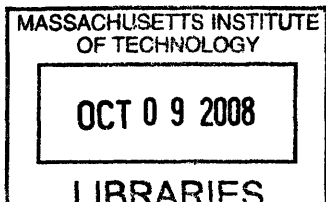
An Investigation of the Mechanics of an Actin Spring

by

Barney Kwun-poo Tam

Submitted to the Department of Physics
on July 30, 2007, in partial fulfillment of the
requirements for the degree of
Doctorate of Philosophy in Physics

Abstract

To produce motion, cells rely on the conversion of potential energy into mechanical work. One such example is the dramatic process involving the acrosome reaction of *Limulus* sperm, whereby a 60-μm long bundle of actin filaments straightens from a coiled conformation to extend out of the cell in five seconds. This cellular engine and the motion it produces represent a third type of actin-based motility fundamentally different from polymerization or myosin-driven processes. The motive force for this extension originates from stored elastic energy in the overtwisted, pre-formed coil-much like a compressed mechanical spring. When the actin bundle untwists, this energy is converted to mechanical work powering the extension.

We investigate the behavior of this actin spring with the identification of an osmotic mechanism controlling the extension and retraction of a helical conformation of the spring. In addition, we measure the bending stiffness of the helical bundle to be $\beta \sim 2.3\pm0.25 \times 10^{-21}$ N$\cdot$m^2 and compare the stored elastic energy to the osmotic work. We stall the retraction of this bundle and find that the required stall force is nearly ~ 8 nN. Furthermore, we stall the acrosome reaction (true discharge) of this actin spring and calculate the maximum force generated by this spring to be nearly 2 nN. To verify this value, we subject cells to a viscous load and characterize the viscosity to independently arrive at a lower bound for the force generated during the true discharge extension. Finally, we detail a mechanism, consistent with experimental observations, which accounts for the role of calcium during extension of the actin spring.

Thesis Supervisor: Paul Matsudaira
Title: Professor, Depts. of Biology & Biological Engineering; Member, Whitehead Institute; Director, MIT/Whitehead Institute BioImaging Center

Thesis Supervisor: Alexander van Oudenaarden
Title: Associate Professor, Dept. of Physics

Acknowledgments

The contents of this thesis could not have been produced without the support of numerous individuals.

I am extraordinarily indebted to Paul and Maha for their insights and guidance;

Jennifer for continual and respectful collaborations;

Guichy, Lera, Danielle, Mekhail, Winston, Mike, Alec, Mariah, Jiayu, and Ricardo for their time in discussing many of the ideas within this work.

Contents

List of Figures

9

10

Chapter 1

Background

The actin spring provides an opportunity to understand a novel motile biological system from a quantitative and mechanical standpoint. The spring generates motion without ATP, and without mysoin, and thus represents a form of actin motility different than that of the traditionally studied systems such as muscle contraction and actin polymerization.

1.1 Cellular Motility

Cellular systems display a bewildering assortment of motion. From the movement of whole cells, to the translocation of individual proteins inside a single cell, motility is a signature property of life. The mechanisms underlying such dynamics are as varied as the motions they produce. Migrating cells exploit the machinery of actin polymerization in a concerted fashion to move from one place to another [1]. Vesicles are transported from one region of the cytoplasm to another via kinesin motors on microtubule tracks [2]. The separation of chromosomes during mitosis is mediated by the assembly and disassembly of microtubules as well [3]. Muscle contraction, a familiar phenomenon, relies on the interplay between myosin molecules and actin filaments [4]. While these processes drastically differ from one another in behavior, molecular engines underlie the motility of all.
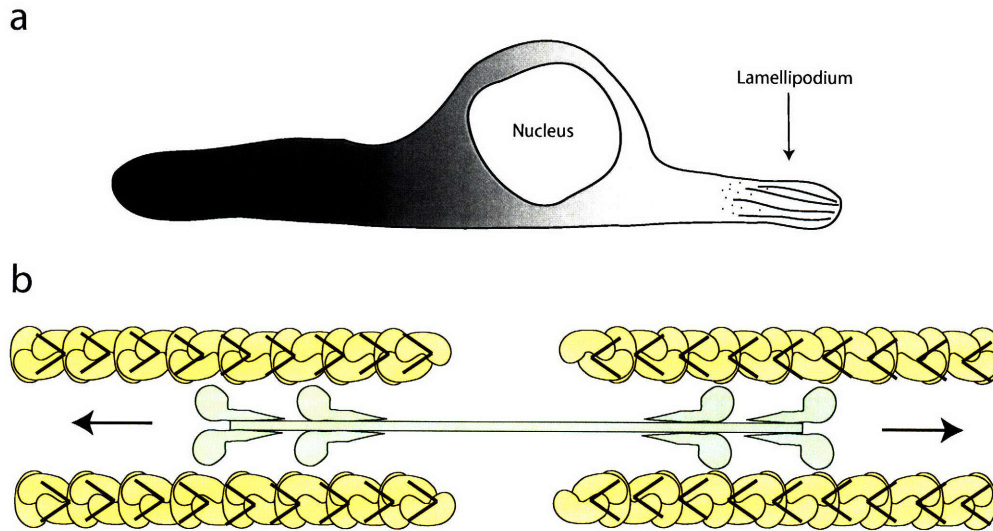
Figure 1-1: Biological Engines. a. Illustration of the actin polymerization machine at the lamellipodium of a migrating cell. The specific power for this engine is $\sim$13 W/kg. b. Active contractile unit of muscle. The myosin heads (green) are arranged in opposing orientation to effect a contractile motion. The specific power of muscle is $\sim$200 W/kg.

1.1.1 Biological Engines

To produce and maintain motion, structures on such a cellular length-scale usually convert chemical energy into mechanical work. By doing so, force is constantly generated. These structures are, in every sense of the phrase, biological engines. In the case of cell migration, a vast network of actin filaments polymerize to push the leading edge, or lamellipodium, of a cell forward (Figure 1-1). Actin polymerization, the engine behind such movement, relies on ATP hydrolysis coupled with thermal motion to produce the pushing forces [5]. ATP is thus required for cellular migration.

ATP is involved in another kind of cellular movement. The force generation associated with muscle contraction involves ATP driving conformational changes of a myosin head, allowing it to move along an actin filament. Chemical energy stored in the phosphate bond of ATP powers the working stroke of the head [6]. Contraction is achieved when myosin molecules are paired in opposing orientation and each pulls on an actin filament. In this motility system, actin plays a passive role by providing the rigid framework myosin needs to produce large-scale motion.

1.2　An Actin Spring

While the two actin-based motility systems mentioned above are extensively studied, there is a third actin-based motile system of biological interest–an actin spring. Found in the sperm cells of *Limulus* crabs, this engine also produces force involved in cell motility. The spring participates in the acrosome reaction of the cell by behaving like a drill, penetrating the protective layers of the egg to initiate fertilization [7]. In contrast to muscle contraction and actin polymerization, however, the energy required to power this motion comes not from ATP, but from twist. Initially, a bundle of actin filaments is coiled and overtwisted from their equilibrium state, effectively storing energy in a manner similar to that of a simple compressed or extended mechanical spring. The release of this strain, i.e. untwisting, fuels the subsequent motion where this actin spring straightens and extends. The conversion of elastic potential energy into mechanical work is unusual in biology and prompts our investigations into this system.

1.2.1　General Morphology and Function

The *Limulus* sperm cell consists of a cell body, an acrosomal vesicle, and a flagella. The cell body is $\sim$4 μm wide and 5 μm long, and is mainly composed of a nucleus. Towards the apical region of the body is an acrosomal vesicle and near the base is attached the flagella. Coiled directly beneath the nucleus is a bundle of actin filaments which make up the acrosomal bundle. One end of this bundle threads through the nucleus via a nuclear channel and abuts the vesicle. The acrosomal bundle resides as a cytoplasmic structure, since it carries with it the nuclear membrane as it coils around the base of the nucleus (Figure 1-2) [8].

When a sperm cell comes into contact with an egg, first the vesicle pops and the acrosomal reaction begins (Figure 1-3) [9]. The acrosomal bundle extends and penetrates the egg via a screwing motion. The motion is in a clockwise sense when viewed from apical to distal. The entirety of the reaction lasts $\sim$5 s with a total length of $\sim$ 60μm. The functional form of the extension is nearly linear (i.e. constant

a   b   c

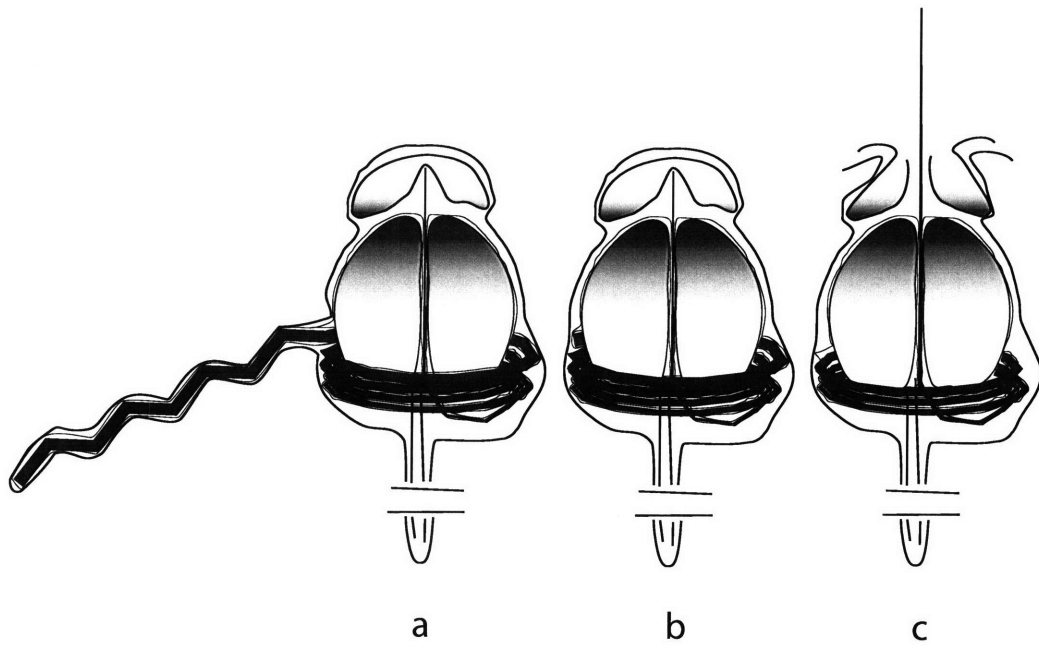Figure 1-2: The 3 states of the acrosomal bundle. a. The false discharge b. the coil and c. the true discharge. Note the gradual tapering of the bundle from the tip to the base, as well as the polygonal nature of the bundle itself. The bundle is sheathed with the nuclear membrane, and hence resides as a cytoplasmic structure. The region where a transition between the TD and coil occurs has a high degree of curvature.

velocity) when induced by ionophore.

While the acrosome reaction is the primary function served by the actin bundle, there is an ancillary reaction which also exists. This secondary reaction, the false discharge (FD), consists of the basal end of the bundle extending obliquely from the base of the cell. The bundle appears with a 2.8 μm sinusoidal shape, and has been observed to occur in hypertonic solutions (Figure 1-4). Another method, perfusing a solution of Triton, a detergent, through a flow cell containing the sperm cells, also induces the FD. The two methods are qualitatively different, as the first technique only extends a portion of the FD, while the latter converts the entire coil into the FD. Triton treatment also disrupts the cell body, eventually bursting the entire cell. Early studies of this reaction have shown that it is indeed helical and not merely sinusoidal, and extends while rotating [10].

1.2.2 Structure & States

The actin spring is composed of actin filaments bound together into a single bundle. This bundle is tapered, with a tip consisting of 15 filaments (24 nm), and a base of 80 filaments (68 nm) [11]. Early work had found that the core filaments themselves had a diameter of $\sim$80 $\mathring{A}$, leading to center-to-center distances between filaments of the same value [7]. Filaments near the periphery of the bundle, however, were measured to be 50 $\mathring{A}$ in diameter. Tilney has speculated that these thinner filaments constitute the ends of the filaments causing the taper of the bundle [7]. Recently, however, workers using cryo-electron microscopy techniques have found that a representative filament has a diameter of $\sim$120 $\mathring{A}$ [12]. Furthermore, the twist in the monomers has been discovered to vary significantly, from -10.4° to 23.6°. The preferred polymerizing end ('plus' or 'barbed' end) of the filaments is apically directed [13]. In unactivated sperm cells, the tip of the bundle lies within a nuclear channel, and the bundle then coils around the nucleus.

To hold the bundle together, each monomer of a filament is decorated with a 102 kD actin-binding protein, scruin. Scruin-scruin interactions are postulated provide the glue holding the strands together [14]. These interactions have also been probed
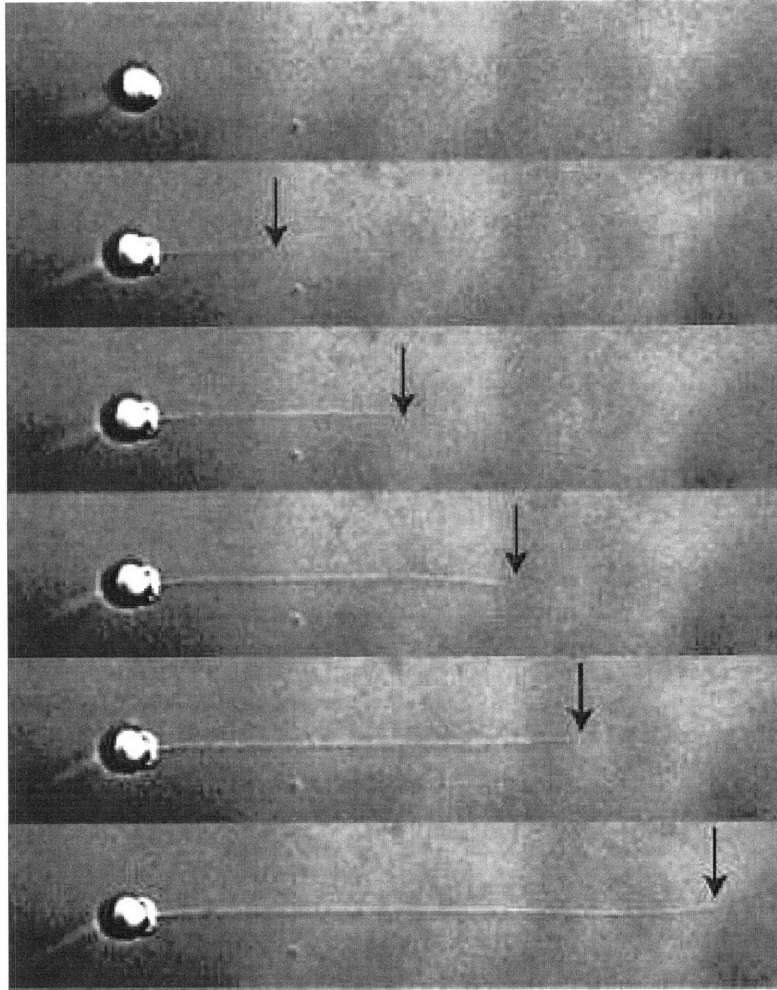
Figure 1-3: A time-series of the acrosomal reaction. Frames are 1.3 s apart. Traditionally, the reaction is triggered using a calcium ionophore, A23187. Motility experiments involve tracking the tip of the extension, as indicated by the arrows. The reaction can complete in $\sim$ 5 s.
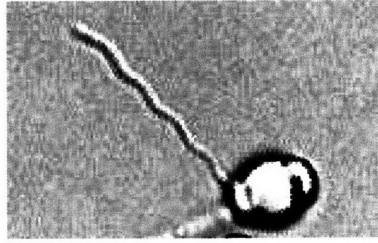
Figure 1-4: The false discharge reaction of the *Limulus* sperm cell. The helical structure is evident. The bundle can typically extend upwards of 15 μm in a reversible fashion.

in vitro through rheological experiments [15]. Direct biochemical evidence of scruin-scruin interactions has not been observed, but the rheological experiments performed by Shin et al. offer compelling evidence of such interactions. Though the crystal structure of scruin has not been determined, electron microscopy studies have shown that it has a bi-lobed structure, with one sphere-shaped lobe connected by a neck region to an elongated lobe. The dumbbell-shaped molecule binds an actin filament orthogonally to its axis. The two domains bind separate actin subunits on the same filament; one lobe binds to subdomain 1 of one actin monomer, and the other binds to subdomain 3 of an adjacent monomer [16]. Each of the scruin domains is composed of a sixfold repeat of a 50-amino acid residue motif, with regions of high hydrophobicity apparent [17]. Bound to the neck region is the 17 kD calcium-sensitive protein calmodulin. One such scruin-calmodulin complex binds to each monomer of an actin filament, resulting in a 1:1 stoichiometry [18].

Scruin binds these filaments together into a hexagonally packed bundle. Though closely packed, this bundle is still capable of significant rearrangement. Indeed, these conformational differences delineate three states of the bundle–the Coil, the true discharge, and the false discharge states. In the unactivated Coil state, the actin bundle exists as coiled structure, wrapping around the base of the nucleus 5-6 times. This coiled conformation is polygonal with 14 arms of 700-nm length, and an equal number of elbows bent at an angle of 154° [7]. The actin filaments in the Coil state are overtwisted by 0.23° per monomer relative to the second true discharge (TD) state. The overtwist is right-handed and is coupled to an overtwist of the entire bundle in

17
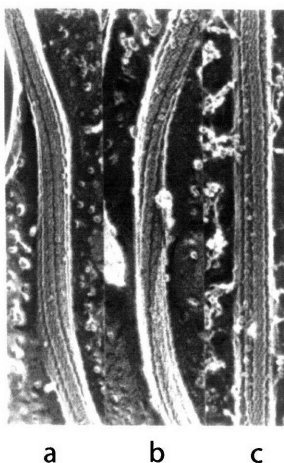
Figure 1-5: States of the Actin Bundle. Frozen and etched segments of the different states of the actin bundle imaged via electron microscopy. a. The false discharge b. the Coil and c. the true discharge. The FD is twisted 30° LH per arm, the coil 60° RH per arm, and the TD is not twisted, without arms [10].

the Coil state. This results in a significant 60° right-handed twist per arm of the coil (Figure 1-5).

Significant structural differences distinguish the Coil state from the TD state. This second state of the actin bundle exists only after activation of the acrosome reaction. The bundle changes from the Coil state to the TD state during the acrosome reaction. In the TD state, the helical rise of each actin monomer is 156° [1]. Moreover, the bundle no longer has elbows, and is shaped essentially like a tapered rod. Upon completion of the acrosome reaction, this rod protrudes ∼60 μm from the apical end of the cell body. Because the TD state exhibits high crystalline order, detailed cryo-electron microscopy has been performed on the bundle in this state [12]. These studies reveal the orientation and position of the actin monomers along with the associated scruin-CaM complex to 9 Å resolution.

The third state, the false discharge (FD) state, too is distinguished by structural differences. The bundle in the FD state is a helical structure which can be induced to extend obliquely from the base of the cell. Again, the bundle begins in the Coil

---

[1]In contrast, unmodified actin filaments are double-stranded, right-handed helixes and have a rotation of 166° per monomer [19].

state, and converts to the FD state. In the FD state, the geometry is of a left-handed discrete helix, and the extension begins from the distal end of the Coil. The FD retains the 700-nm straight segments found in the Coil, but no longer exhibits an overtwist of 60° per arm. Instead, the FD is twisted 30° in a left-handed manner. This twist results in a -0.11° deviation per monomer relative to the TD state. As a consequence, the large-scale structure of the bundle in the FD state is not that of a coil, but of a helix, with a period of 2.8 μm corresponding to 4 arms and elbows. The elbows retain the 154° bend as in the Coil, however [10].

Once converted to the TD state, the actin bundle has not been observed to return to the Coil state. The FD state has been observed to extend and retract, though no systematic experiments have been described in the literature. Since the handedness of the FD is opposite from that of the Coil, and yet transitions occur between the two states with ease, there must exist a transition state where there is no handedness to the actin bundle. A change from left-handed chirality to right-handed chirality cannot occur otherwise. Such a state has not currently been observed.

1.2.3 The Role of Calcium

Calcium is crucial to the acrosome reaction. The traditional method of activating the TD has been with the calcium ionophore A23187. This calcium-carrier molecule equilibrates the intracellular calcium concentration with the external concentration, thereby introducing excess calcium ions to the acrosome bundle. The mechanism by which this equilibration occurs has been well documented in a model system [20, 21]. A23187 complexes with a Ca^{++} ion in a 2:1 ratio and facilitates the exchange of the ion for two protons. This complex then breaches the hydrophobic membrane by circumventing the layer of water molecules usually surrounding ions, and mediates the exchange. Though detailed, this mechanism fails to account for the heterogeneity seen inside biological systems. Such heterogeneity, i.e. organelle structures, microdomains of different ion concentrations, various layers of membrane, could qualitatively interfere with the ionophore function. Regardless of this fact, A23187 has been used to trigger the acrosome reaction [7, 22].
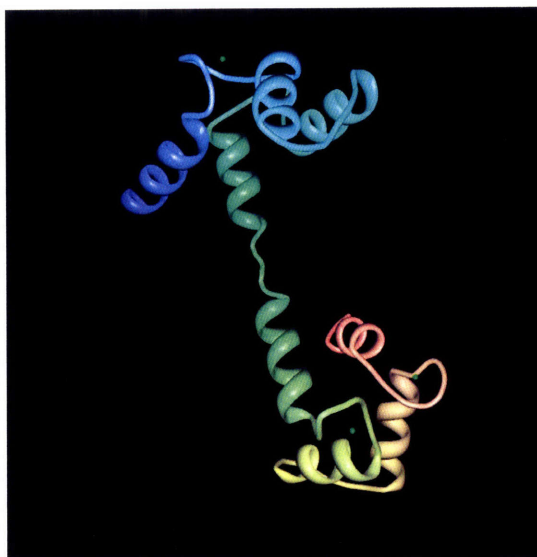
Figure 1-6: Structure of Calmodulin, a calcium-sensing protein. A representation of the protein calmodulin (CaM) created by the Molecular Biology Toolkit [25]. The green spheres represent bound calcium ions. Calcium binding induces large conformational changes in the protein. Specifically, binding induces the open conformation of CaM which result in the exposure of hydrophobic patches on the protein.

Once the calcium ions are within the cell, however, they are able to bind to a calcium-sensitive protein found in large amounts decorating the bundle. The well-studied calcium-sensitive protein, calmodulin (CaM), is found in a 1:1 ratio with scruin in the bundle [18]. CaM is nearly ubiquitous in eukaryotes, and is highly conserved. It has four E-F hands, forming two globular domains joined by a flexible linker region [23]. The structure of CaM has been determined to 2.2 Å (Figure 1-6) [24].

Each E-F hand binds one calcium ion. Though CaM has multiple sites with which to bind calcium, biochemical studies have shown that no cooperativity exists between the two globular domains, though positive cooperativity was detected for calcium binding within each domain [26]. Moreover, the affinity for calcium is nearly six-fold higher at the C-terminal domain than at the N-terminal one. Such characteristics are highly suggestive that CaM is able to modulate the various reactions associated with the acrosomal bundle.

With four binding sites for calcium ions, this molecule is believed to trigger the

acrosome reaction upon binding to calcium. CaM has been shown to exhibit conformational changes upon binding to calcium [27, 28]. The binding of calcium induces changes within the E-F hands, which lead to an open conformation. Indeed, interhelical angle changes of up to 44° and E-F-hand helix distance changes of 6.2 Å have been observed [29]. Such conformational changes also modulate the exposure of hydrophobic patches on CaM [30].

Calcium binding kinetics of the FD and TD have been investigated via isothermal titration calorimetry (ITC) and have revealed two accessible sites for both conformations [31]. With such demonstrated calcium sensitivity in vitro and in the FD and TD, it is believed that CaM confers upon the scruin-CaM complex the ability to induce the macromolecular conformational changes required during the acrosomal reaction.

Though calcium binding is required in activating the acrosome reaction, the free energy attributed to calcium binding is not sufficient to power the extension when compared to the energy dissipated through viscous drag and friction. The possibility that calcium binding is a potential energy source for extension has been eliminated by the ITC experiments.

1.2.4   Energetics

An energy source for motility is suggested by the overtwist of actin monomers in each filament. This overtwist is coupled to an overall overtwist of the entire bundle. In the coiled bundle, each monomer is overtwisted by 0.23° relative to an adjacent monomer, leading to significant energy being stored elastically. This twist displays a right-handed chirality and is absent in the TD conformation of the bundle. For the FD conformation, the chirality is left-handed, and the twist is -0.11° [10]. For the bundle in the TD state, a measurement of the bending stiffness and thus the Young's modulus has been obtained using hydrodynamic flow [11]. The average Young's modulus from these measurements was ~2 GPa, similar to hard plastic. Surprisingly, this value is very similar to that of single actin filaments, indicating that scruin-scruin interactions provide rigid cross-linking [15, 32]. From this, an estimate of the stored

energy has been determined using elementary elasticity theory [31]. The resulting value of $\sim 10^{-13}$ J is significantly larger than the energy provided by calcium binding.

1.2.5 Theoretical Model

Simple mechanical springs store energy via compression or extension. Mathematically, this yields an expression for the stored energy, $U = 1/2kx^2$, where x is the displacement of the spring from its equilibrium position. From this equation, we can find the force resulting from the displacement by taking the negative gradient of the energy, $F = -\nabla U$.

Likewise for the actin spring, we can formulate a mathematical description of the system by considering the twisting strain of the filaments as a natural order parameter [33]. Since the bundle prior to calcium binding exists as different conformational states parameterized by the twist, i.e. FD state is overtwisted -0.11°/monomer whereas the coil state is 0.23°/monomer, the simplest functional form representing these states as local minima of the potential is that of a double well. Upon calcium binding, the only state remaining is the calcium bound, twisted coiled state, which releases its energy to transition into a global minimum state, the TD. This bound calcium state can be described by a traditional quadratic term in the twist. The depths of the wells are experimentally determined, and both wells in the double well potential are assumed to have similar values. The bound calcium TD state is assumed to be a global minimum, owing to the fact that no transition away from the TD state has ever been observed.

We describe the system mathematically with the following expression for the energy

$$E = \int \left[V(\Omega) + \frac{Cr^2}{2}\Omega_x^2 \right] dx. \tag{1.1}$$

Here $V(\Omega)$ represents the potential parametrized by the twist $\Omega = \phi_x$, for either the FD-Coil double well, or the TD single well (Figure 1-7). $\phi(x,t)$ is defined to be the angle which individual filaments make with the tangent to the centerline of the bundle. The second term, $\frac{Cr^2}{2}\Omega_x^2$, represents the width of the interface between the

22
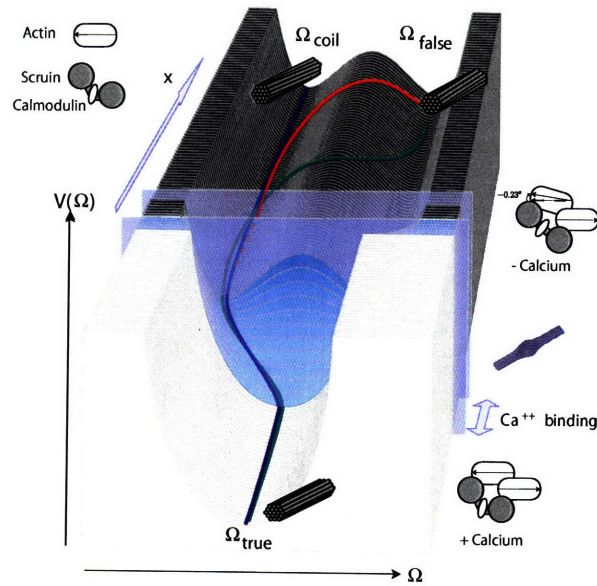
Figure 1-7: Energy Landscape of an Actin Spring. Energy landscape governing the behavior of the actin spring. The two locally stable conformations of the actin spring in the absence of calcium, the coil and FD states, are represented as local minima of a double well potential in the figure. The globally stable, calcium induced TD state is represented as the single well potential. The region connecting the two potentials exhibits a non-zero twist gradient, and hence provides a preferential region for calcium to bind to calmodulin. The entire system is parameterized by the twisting strain, Ω.

two wells. The constant, C, is related to the torsional rigidity of the bundle, and r is the bundle radius.

In a similar fashion to the simple mechanical spring, we can obtain a local balance of torques, and hence dynamics for the actin spring if we consider frictional effects resulting from interfilament interactions [34]. Such calculations are detailed in Mahadevan et al. and constitute the theoretical motivations of the experiments described in the proceeding pages.

Chapter 2

Investigating a Helical Actin Bundle

The false discharge (FD) reaction offers an avenue to probe the motion of the actin spring. Because experiments on the coil state remains out of reach, the FD, with its similar conformational properties, provides a means of investigating the actin spring in an easy manner. Insights gained from the FD reaction are useful to understand the mechanics and behavior of the actin spring in general.

2.1   FD Energetics

We report on a mechanism to control the extension and retraction of the FD. Previous studies have only described the qualitative features of the extension, and do not provide a means to regulate the FD. By identifying an osmotic mechanism inducing the FD, we are able to investigate quantitatively the behavior of the FD in a controlled and reversible manner. The FD can extend to an average length of 15μm under different solutes, irrespective of the solute causing the extension.

In addition, we describe hydrodynamic loading experiments performed on the FD structure to determine the potential energy stored. Springs store energy because the materials they are composed of are elastic. A strain deformation of a spring from its equilibrium conformation stores potential energy. In the case of a simple helical

mechanical spring, such a strain is comprised of a compression or extension. For the actin spring, however, the energy is stored in the twist of individual filaments. Though the manner in which the spring deforms is different in each case, the material property govering the amount of energy stored is the Young's modulus, E, in both cases. Measurements of the bending stiffness, β, of the helical bundle provide a means of determining E. We bend the actin bundle via hydrodynamic flow and measure the displacement from equilibrium. From these experiments, we find $\beta \sim 2.3 \pm 0.25$ x 10^{-21} N·m^2. These experiments indicate that the bending stiffness, and hence, E, of the helical actin bundle is less than that of the straight bundle.

To bend the FD bundle, we induce the extension of the FD state. This arrangement provides a geometry in which there is a fixed point to serve as an anchor for the bending analysis. This point is located at the base of the cell where the FD first exits the cell body. We approximate the FD bundle as a simple beam for the bending analysis since the helical radius:length is small, so the significant component of bending is due to deflection, and not twisting of the bundle.

We begin with a derivation of the beam equation [35]. For a slender, isotropic, and homogeneous rod bent into a circular arc, the curvature of the rod, κ, is simply related to the bending moment, M, by the equation

$$M = EI\kappa \qquad (2.1)$$

where the constant of proportionality, EI, or β as it is sometimes found in the literature, is called the bending stiffness of the rod. Here, E is Young's modulus of the material, and I is the second moment of inertia. E is solely a property of the material (i.e. it is independent of the rod geometry), whereas I is purely determined by the geometry of the rod cross section. We can relate the radius of curvature, R, to the arc length with the relation, $d\theta/ds = 1/R$, where θ is the tangent angle associated with the arc length (Figure 2-1).

For small angles, we can transform the beam equation to Cartesian coordinates with the following approximations: $x \cong s, dy/dx \cong dy/ds = sin\theta \cong \theta$. We arrive at
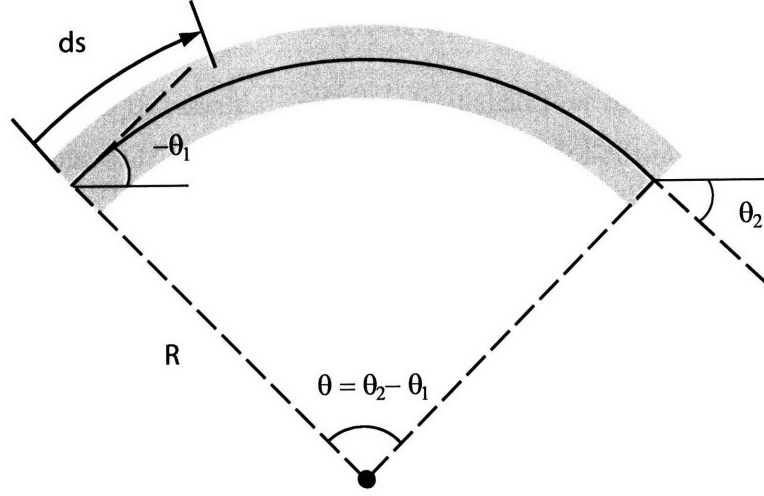
Figure 2-1: Beam Diagram. Geometry of beam bending used to derive beam equation.

the beam equation

$$\frac{d^2y}{dx^2} = \frac{M}{EI}.$$ (2.2)

When we specialize to a particular bending moment, that of a uniform distributed load in the form of a hydrodynamic drag force, we can apply force and torque balances to arrive at

$$f_{drag} = EI\frac{d^4y}{dx^4},$$ (2.3)

where f_{drag} is the frictional drag force per unit length on the rod [36]. Drag forces are typically characterized by a drag coefficient, ξ, multiplied by the velocity of the fluid acting on the object. The drag coefficient has been calculated to be

$$\xi_{cyl}^{\perp} = \frac{4\pi\mu}{\ln(2h/r)}$$ (2.4)

for transverse motion of a cylinder near a surface [37]. Here, μ is the fluid viscosity, h is the height of the cylinder above the surface, and r is the cylinder radius. Substituting, and solving the differential equation with appropriate boundary conditions, we obtain

27

the final expression for the deflection of a cylinder under hydrodynamic loading

$$y(x) = \frac{\pi \mu v}{\ln(2h/r)} \frac{L^4}{6EI} \left[\left(\frac{x}{L}\right)^4 - 4\left(\frac{x}{L}\right)^3 + 6\left(\frac{x}{L}\right)^2 \right]. \tag{2.5}$$

From this equation, we calculate the bending stiffness, β, and the resultant elastic energy stored in the FD bundle. We can then compare this value to the work done by osmotic pressure, and the energy stored in the coiled state.

Methods & Materials

Osmolarity Experiments: Sperm cells were collected from live crabs and washed once with artificial sea water (ASW: 423 mM NaCl, 9 mM KCl, 9.27 mM CaCl$_2$, 22.94 mM MgCl$_2$, 25.5 mM MgSO$_4$, 2.15 mM NaHCO$_3$, 10 mM Tris, pH adjusted to 7.9-8.0). A 1-μL sample was then diluted 1000-fold with ASW and injected into flow chambers constructed from No. 1.5 Corning coverslides and double-stick tape. In order to immobilize the cells, coverslips were first treated with a 2% (v/v in acetone) solution of the non-specific tissue adhesive, Biobond, for 4 min and then rinsed with Millipore ddH$_2$0.

Increasing concentrations of NaCl or glucose supplemented ASW solutions were then flowed through the chamber. A series of solutions were prepared with ASW in 100 mM increments of excess NaCl or glucose. DIC video microscopy was used in tandem with Improvision OpenLab software to collect and analyze data. The dynamics of the FD extension was recorded using a SVHS-VCR recording at 30 fps and digitizing the clips to a PC. Tracking analysis was performed using a program developed by Photron USA Inc (San Diego, CA).

To measure the osmolarity of a solution, an osmometer (Model 5520 Vapor Pressure Osmometer, Wescor, Logan, UT) was used. Each solution was measured three times, and the osmolarity of a solution was determined as a function of solute molarity. Conversion factors were obtained for NaCl and glucose and used to make the constant osmolarity solutions. For the constant osmolarity experiment, the osmolarity (total solute concentration) of the solutions was held constant at ~ 1250 mOsm.

This was accomplished by using a series of solutions composed of both NaCl and glucose, with PBS as the base solvent instead of ASW. For a given concentration of NaCl, a complementary amount of glucose was added to bring the total osmolarity to 1250 mOsm.

Hydrodynamic Loading: All experiments were performed under a Nikon TE-300 inverted microscope with a 100X (NA 1.4) objective using DIC optics and recorded with a CCD camera. The same flow chambers from the osmotic pressure experiments were used. After cells were adhered to the surface, a 10% casein solution in 600 mM NaCl in ASW was flowed in to extend the FD and to prevent the FD from non-specific surface interactions during the experiment. Then 600 mM NaCl in ASW was flowed through the chamber to bend the bundle. To generate flow, filter paper (Whatman, #54, NJ) was used to draw the solution through the chamber. The velocity of the fluid flow was determined by tracking 200-nm diameter polystyrene beads added to the solution. The viscosity of the buffer was measured with a Cannon-Fenske Routine viscometer.

Results & Discussion

To probe the behavior of the FD reaction, we changed the osmolarity of the ASW solution in which sperm cells were natively immersed. We measure the osmolarity of the solutions in milli-Osmols to determine the effect such a change has on the FD in a consistent manner. Measurements of the osmolarity of the solutions indicate a linear relationship between molar concentration and osmolarity (Figure 2-2).

With these high osmolarity solutions, we probed the behavior of the FD under osmotic pressure. In ASW, no significant extension of the FD is observed. When we flowed solutions of higher osmolarity through the chamber in a stepwise fashion, the FD extended incrementally (Figure 2-3).

We measured the extended FD lengths for 10 cells in a set of experiments and correlated that to the total solution osmolarity. Lengths were measured from the base to the tip of the FD. For both NaCl and glucose, a similar trend is observed (Figure 2-4). We note that a plateau of 15 μm FD length is reached at $\sim$2000 mOsm.

29
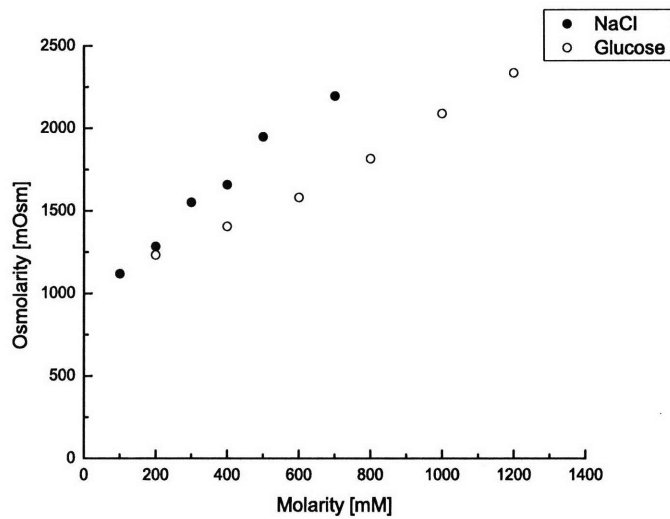
Figure 2-2: Osmometry Measurements of NaCl and Glucose. The graph shows the linear trend of Osmolarity as a function of molar concentration of the solutes. The solvent in both cases is ASW, with an osmolarity of ~ 960 mOsm. Linear best-fit analysis yield a conversion factor of ~ 1.1 mOsm/M for glucose, and ~ 1.8 mOsm/M for NaCl.
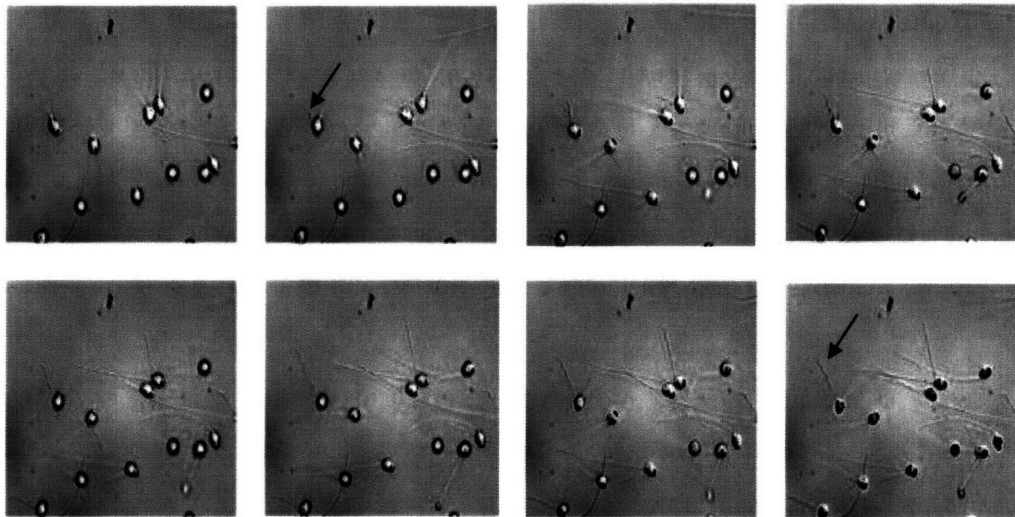
Figure 2-3: FD Extension Series. This series of images shows the extension of the FD increasing as the amount of NaCl is increased. NaCl concentrations supplemented in ASW range from 0mM to 700 mM in 100 mM increments beginning from upper left image. Arrows point to the FD extension.

30
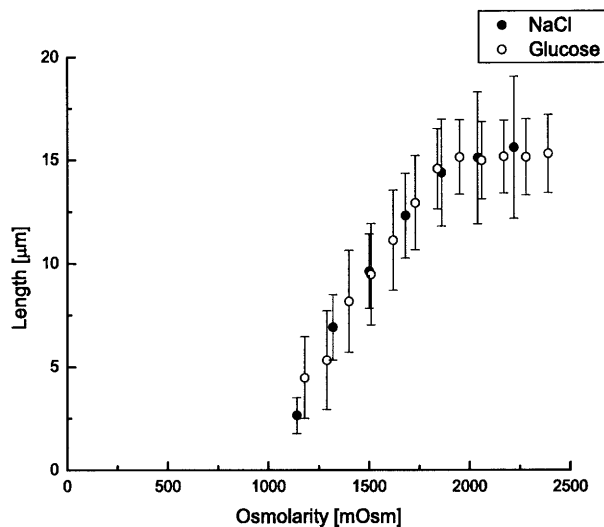
Figure 2-4: FD Extension. Length of the FD extension plotted as a function of osmolarity. The two solutes used to extend the FD, glucose and NaCl, resulted in nearly identical behavior when compared on the basis of osmolarity instead molar concentration.

The extension as a function of osmolarity appears to be linear. We perform a linear best-fit analysis on the regions exhibiting FD extension to determine the slope. For the glucose set of experiments, we find a slope, k, of 0.015 μm/mOsm, with $r^2 = 0.98$. We calculate similar values for the NaCl set of experiments: a slope of 0.016 μm/mOsm, and $r^2 = 0.98$. The FD fully retracts when we flow ASW back into the chamber. However, when we stepwise decrease the osmolarity, we do not observe a stepwise shortening of the FD. For a given extension length, we are able to fully and reversibly extend and retract the FD upwards of 3 to 4 times.

We performed constant osmolarity experiments to further test if osmotic pressure was the driving force behind extension and retraction. At $\sim$ 1250 mOsm, the FD extends an appreciable amount ($\sim$ 5 μm), enough to observe additional extension when flowing the different solutions through the chamber. If the extension responded to absolute concentrations of either NaCl or glucose, additional extension should be observed as the NaCl or glucose component in the solution increases. However, a mechanism which responds to the total osmolarity of the solution would not exhibit any additional extension. The FD did not extend or retract significantly as the salt

31

concentration was increased, or conversely as the glucose concentration was decreased.
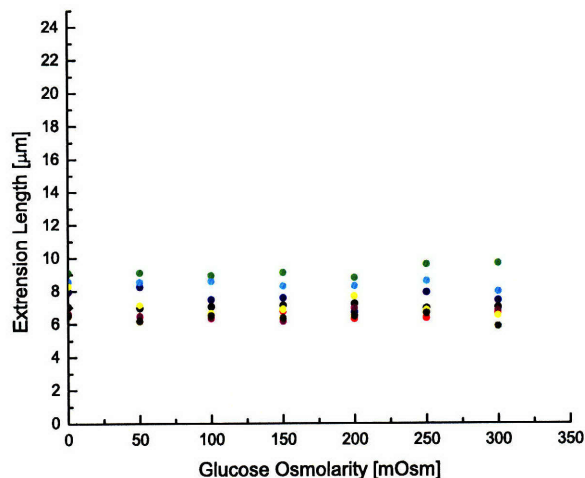
Figure 2-5: Constant Osmolarity Experiment. Each set of colored dots represents one cell. The total osmolarity of the solution was held constant at 1250 mOsm while varying the two principal solutes, glucose and NaCl. Cells were then exposed to the solutions and the FD extension was monitored.

Because the FD extension is a dynamic process, we also investigated the time dependent behavior of the extension. We chose to use solutions having an osmolarity of ~ 2000 mOsm to produce the FD extension. Such an osmolarity results in an extension of sufficient length to analyze its time dependence. We consider the extension under 4 different conditions: using NaCl, glucose, NaCl in 50 mM $CaCl_2$ ASW, and NaCl in zero-Ca^{++} ASW. For each condition, we analyzed 9 individual cells to determine their retraction trajectories and average velocities. We find that, within the standard deviation from the samples, the average velocity appears to be unaffected by the kind of solute used to effect the retraction.

We also investigated the temperature dependence of the FD extension. No extension was seen over the temperature range we used. We increased the temperature for the flow chamber in ten degree steps, from 4-44° C, but observed no extension. An additional experiment consisting of simply heating a dilute solution of cells to 50° C again induced no extension.

A calculation based on the osmotic pressure relation $P = cRT$, where c is the total solute concentration, reveals that the pressure difference caused by a temper-
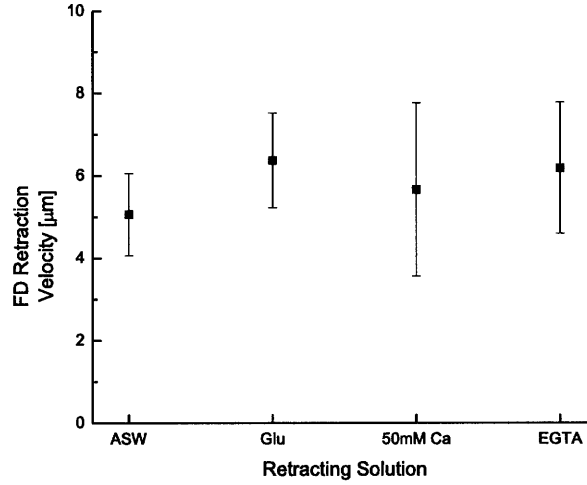
Figure 2-6: FD Retraction Velocity. Average retraction velocities of FD induced with various solutions. There is little variation between different extending media, suggesting that the extension is independent of the solution causing the solution. This is consistent with an osmotic pressure as the driving force behind the extension.

ature differential is an order of magnitude less than a pressure difference caused by a concentration differential. Thus, it is likely that the temperature difference is not strong enough to induce extension.

Because we are able to quantify the pressure acting on a single cell, we can calculate an upper bound for the work done on the cell in extending the FD due to the additional solute concentration. We take the osmolarity at ASW to be isoosmotic to the cell, since no FD extension is observed at this value. We use the volume from the extended FD ($\sim$ 15 μm) induced by a 600 mM NaCl ASW solution for our calculation. The osmotic pressure is held constant because there is no volume change within the cell, only a redistribution of the volume from the cell body to the FD extension.

$$
\begin{aligned}
\mathrm{d}U_{osm} &= P\mathrm{d}V \\
&= cRT\pi r^2 \mathrm{d}L \\
&= cRT\pi r^2 k\mathrm{d}c \\
U_{osm} &= \int_0^{L/k} cRT(r_{max}^2 - 2skcr_{max} + s^2k^2c^2)\pi k\mathrm{d}c
\end{aligned}
\tag{2.6}
$$

33
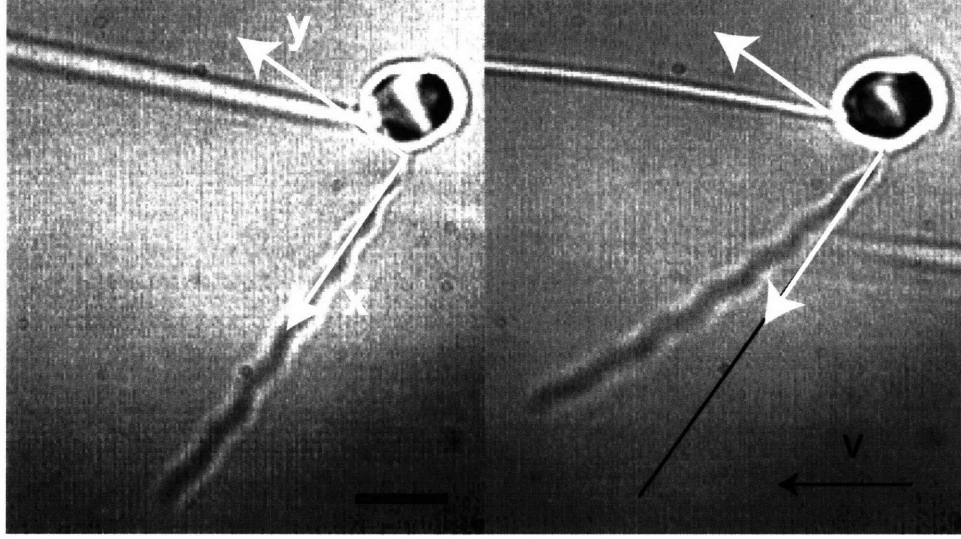
Figure 2-7: Deflection of FD under Hydrodynamic Load. The left image depicts the straight FD in equilibrium. The right image shows the bundle deflecting due to fluid flow. The coordinate axes for the bending analysis are in white. The direction of the fluid flow is indicated by the velocity vector, v. Scale bar is 5 μm.

$$= RT\pi k \left(\frac{L^2 r_{max}^2}{2k^2} - \frac{L^3 2skr_{max}}{3k^3} + \frac{L^4 s^2 k^2}{4k^4} \right) \qquad (2.7)$$

$$\simeq 4.3 \times 10^{-16} \text{ J} \qquad (2.8)$$

Here, c is the osmolarity of the external solution, R is the universal gas constant, T is the temperature in Kelvin, and k is the slope calculated earlier. The constant, $s = 0.0073$, is the taper of the bundle. The resulting energy represents the work done by the osmotic pressure over a volume equivalent to the extended FD.

For comparison, we determined the elastic energy stored in the FD conformation by measuring its bending stiffness. We performed hydrodynamic loading experiments on 8 cells and measured the deflection y of the FD from its equilibrium position as a function of the bundle coordinate, x(Figure 2-7). The cause of this deflection is the flowing fluid which places a uniformly distributed load along entire exposed bundle.

We tracked a 200-nm diameter polystyrene bead for several frames in order to determine the velocity of the fluid (Figure 2-8). We then take the perpendicular component of the velocity as that which causes the distributed loading on the bundle.
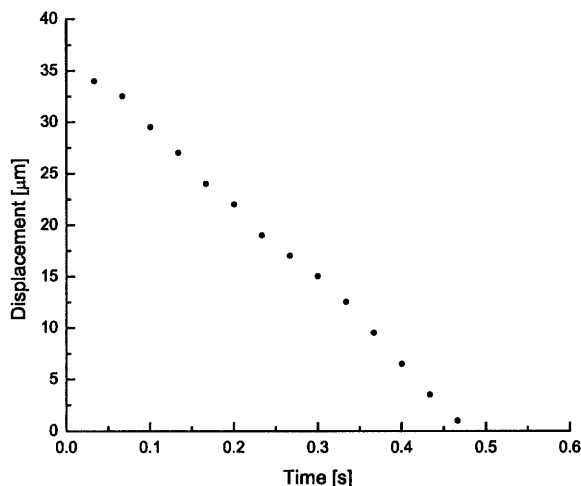
Figure 2-8: Bead Displacement. Horizontal displacement of tracer bead used to determine fluid velocity. The linear behavior indicates a constant bead velocity.

With the velocity, viscosity, and deflection curve known, we calculate the bending stiffness for a given bundle.

We use Equation 2.5, where we have taken $h = 1$ μm, and μ=0.0016 Pa·s. The significance of the taper of the bundle is slight when calculating the bending stiffness due to a distributed load, so we use an average radius of $r = 62$ nm. To obtain each of the deflection curves, we measured 7-10 points along the central axis of deflected bundle to an accuracy of 0.4 μm. From each point, we calculate the associated bending stiffness of the bundle, and then average the results for each sample. We then calculate the deflection curve associated with the measurements (Figure 2-9).

Our analysis results in $\beta \sim 2.3 \pm 0.25$ x 10^{-21} N·m^2. From this value, we extract the elasticity of the bundle when in the FD state. We find that $E = \beta/I \sim 1.2$ x 10^8 N/m^2. Such a value is an order of magnitude less than that found for the TD [31].

We have used two independent methods to probe the energetics of the FD reaction. We compare the elastic energy stored in the bending of the FD to the work done by the osmotic force. To calculate the elastic energy stored in the FD, we begin with $U \simeq \beta\tau^2 L/3$, where τ is the twist per unit length. Since the energy is a function of length, and the bending stiffness also, we integrate to find the total elastic energy

35
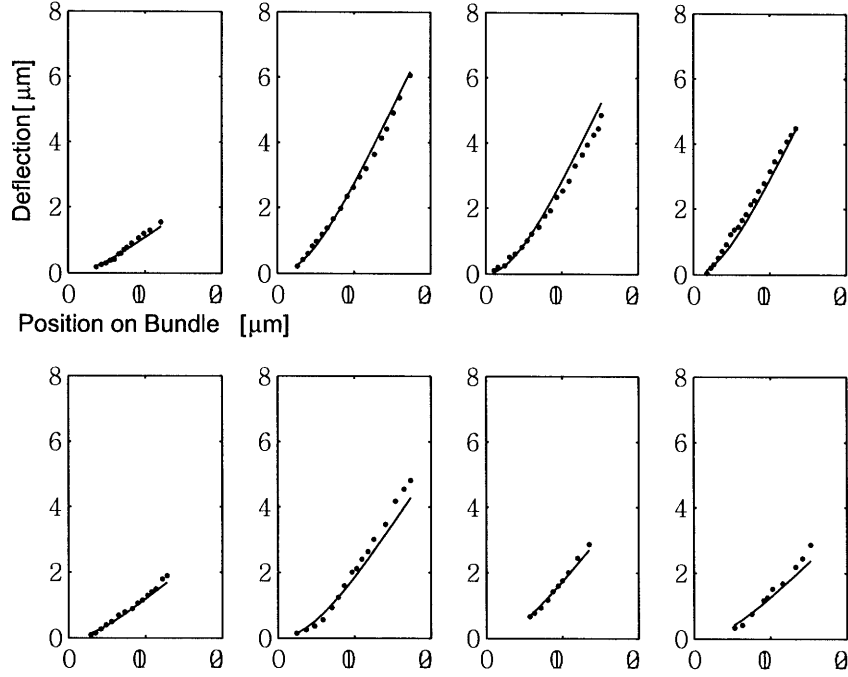
Figure 2-9: FD Deflection. Individual deflection curves for single cell bending experiments. The solid circles are the empirical results, and the solid lines represent calculated deflection curves derived from the bending stiffnesses.

stored in the FD conformation for a 15-μm length of the bundle. We have

$$
\begin{aligned}
dU &= \frac{EI(r)\tau^2 dl}{3} \\
U &= \frac{E\pi\tau^2}{12} \int_0^L (r_0 + cl)^4 \, dl \\
&= \frac{E\pi\tau^2}{60c} \left[(r_0 + cl)^5 - r_0^5 \right] \\
&= 4.5 \times 10^{-15} \text{ J}
\end{aligned}
$$

(2.9)

(2.10)

The work done by osmotic pressure, U_{osm}, is $\sim 4.3 \times 10^{-16}$ J. The stored elastic energy in the FD is nearly an order of magnitude greater than U_{osm}. With such values, we quantitatively complete the energy landscape presented in Chapter One. We find that the two wells of the double well potential are comparable in energy relative to the

TD*

$U \sim 10^{-15}$ J

Coil

FD

$U \sim 10^{-16}$ J   Ca^{++}

$U \sim 10^{-13}$ J

TD
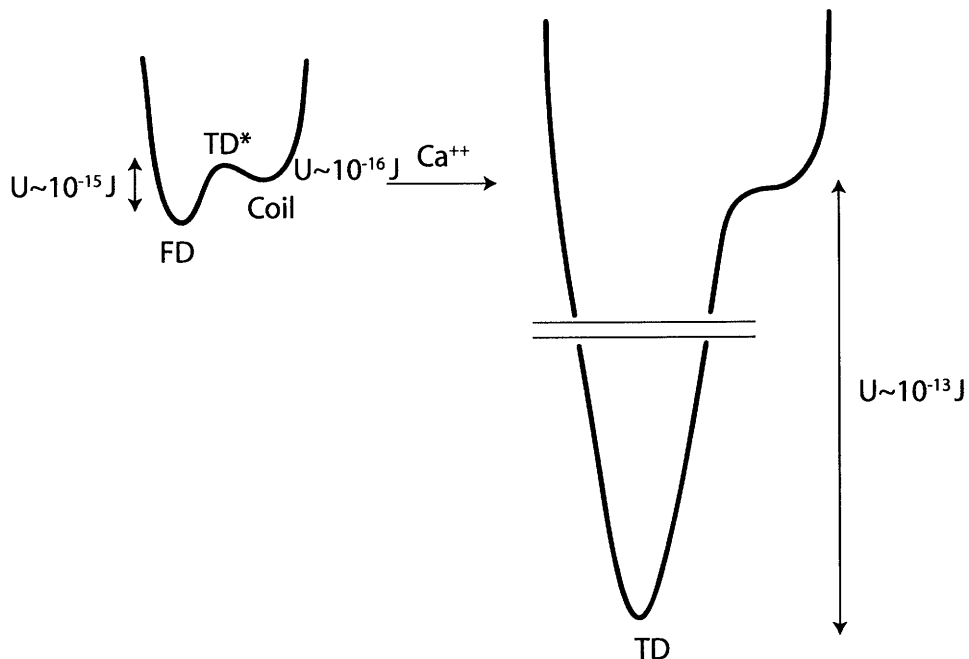
Figure 2-10: Values for the energies were calculated for a 15-μm segment of the bundle.

stored energy in the coil, and that the minimum state postulated for the TD is global, with an energy of $\sim 10^{-13}$ J (Figure 2-10). This verifies two of the assumptions built into the theoretical model of the actin spring [33].

2.2 Retraction Force

We find an estimate of the retraction force for the FD reaction by embedding cells in agarose (this technique and the analysis accompanying it are described in Chapter Four). For cells embedded in a 3% agarose mix, we calculate that the average shear drag force opposing motion is ~ 8 nN.

Methods & Materials

100 μL of sperm cells were collected and washed in 500 μL ASW. Aliquots were diluted to 1:1000 and solutions flowed into flow chambers described previously. The FD was extended using 600 mM NaCl in ASW. A molten 3% solution of agarose in

600 mM NaCl ASW was then flowed through the chamber, and then the chamber was cooled at 4° C for 15 min. Cells were induced to retract the FD by irradiating a section of the flagella in the exact manner as described in Chapter Four. Video was captured and analyzed using a PC.

Results & Discussion

By embedding cells in agarose, we are able to stall the FD retraction. We measure the length of the FD when it stalls, and use the average radius of the bundle r_a, and the stall length L_s to calculate a stall force, F_s associated with the experiment.

$$F_s = F_{drag} = \tau 2\pi r_a L_s \qquad (2.11)$$

We take $\tau = 1.7 \pm 0.3$ kPa from our agarose characterization experiments in Chapter Four. The radius we take to be $r_a = 62$ nm, and the lengths from the indicated stall regions (Figure 2-11), we find that the stall force $\sim 8 \pm 4$ nN. This is nearly four times larger than the force generated by the true discharge. This can easily be understood, since the radius of the coil generating the FD is over twice as large as that generating the TD. The actin bundle generates force proportional to the amount of material undergoing the reaction, be it a transition from coil-to-TD or FD-to-coil.

2.3 Global Rotation of Coil

We label the actin bundle with Texas Red-phalloidin to investigate structural changes of the entire bundle during the FD extension. We find that the section of the bundle within the nuclear channel remains even after extension of the FD. Since the bundle is one connected entity, this result indicates that the bundle undergoes a global rotation during the FD extension.

Methods & Materials

100 μL of sperm cells were collected and washed in 500 μL of ASW. Aliquots were
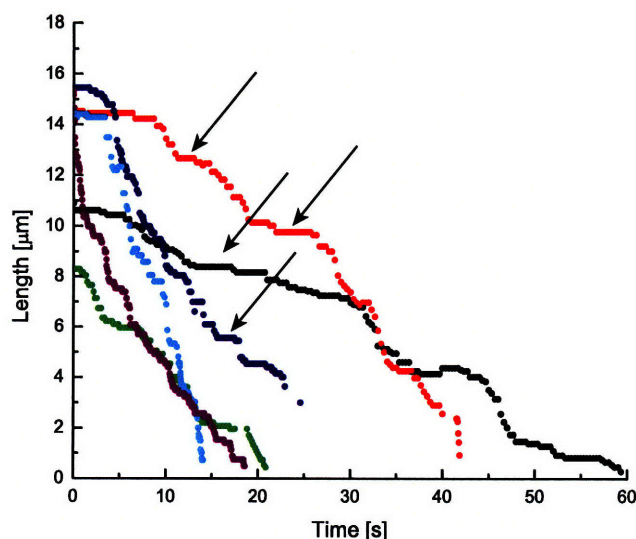
Figure 2-11: FD Retraction Stalling in Agarose. Tracking data for cells embedded in 3% agarose and induced to retract the FD. The arrows indicate regions on the plot where the FD completely stalled. Knowing the length of the stall allows a calculation of the frictional shear drag force which produced the stall.

diluted to 1:1000 and solutions flowed into flow chambers described previously. The FD was extended using 600 mM NaCl in ASW and then fixed the cells using a 2% (v/v) of Paraformaldehyde in ASW. After fixing for 5 min, cells were exposed to 0.01% Triton in ASW for 5 min to remove the plasma membrane. Upon completion, cells were washed once with ASW, and then a 1:1000 dilution of Texas Red-Phalloidin in ASW was flowed thru to label the actin bundles. After a 15 min incubation, ASW was flowed thru the chambers to remove excess dye. Cells were imaged with a TE-200 Nikon Inverted Microscope using a 100X (1.4NA) and a Rhodamine filter set.

Results & Discussion

We label the actin bundle using Texas-Red phalloidin (Figure 2-12). The dye binds to the entire bundle, including regions in the FD and TD states. Because the FD and TD states reside on the same bundle, our result indicates that the coil undergoes a global rotation as the FD extends, and provides further evidence that the FD reaction occurs at a localized region.

Local extension of the FD has been suggested by DeRosier [10], with the coil

39

Figure 2-12: Actin bundle labeled with TR-phalloidin. The complete labeling of the bundle indicates that the bundle rotates as the FD extends.

changing handedness as the FD extends. This extension involves a change in the twist of the bundle, from -30° to 60°. Since the TD section of the bundle remains fixed in the nuclear channel, the only mechanism allowing for extension of the FD is one in which the entire coil rotates as the FD extends.

2.4 Straight FD Conformation

We investigate the occurance of a novel conformation of the actin bundle. By demembranating cells with Triton X, a detergent, in the absence of calcium, we discover a straightened conformation of the actin bundle. We image these bundles using transmission electron microscopy, to find a helical interfilament geometry.

Methods & Materials

100 μL of sperm cells were collected and washed in 500 μL of ASW. A 10 μL aliquot of cells were suspended in 990 μL zero-Calcium ASW solutions with 0.1 mM EGTA and 0.01% (v/v) Triton X-100 detergent. Upon incubating at room temperature for

30 min, the solution was then placed on an EM grid and imaged.

Results & Discussion

We extracted the straightened FD bundle using a simple detergent mix in zero-calcium ASW. In about 30% of the recovered actin bundles, the conformation differed from the expected helical FD conformation. Instead, we found a straightened conformation with a twist apparent in interfilament structure (Figure 2-13).

The discovery of this straightened structure conflicts with established theory, since we have postulated that a straightened TD conformation only arises from calcium rich environment. A possible explanation for this structure involves a metastable TD structure with no calcium ions bound. Such a structure can be accomodated in the theory, since the transition between FD and Coil states demands an intermediate state with no twist. However, such speculation requires more evidence to substantiate. Further investigation is needed to verify and understand this conformation.
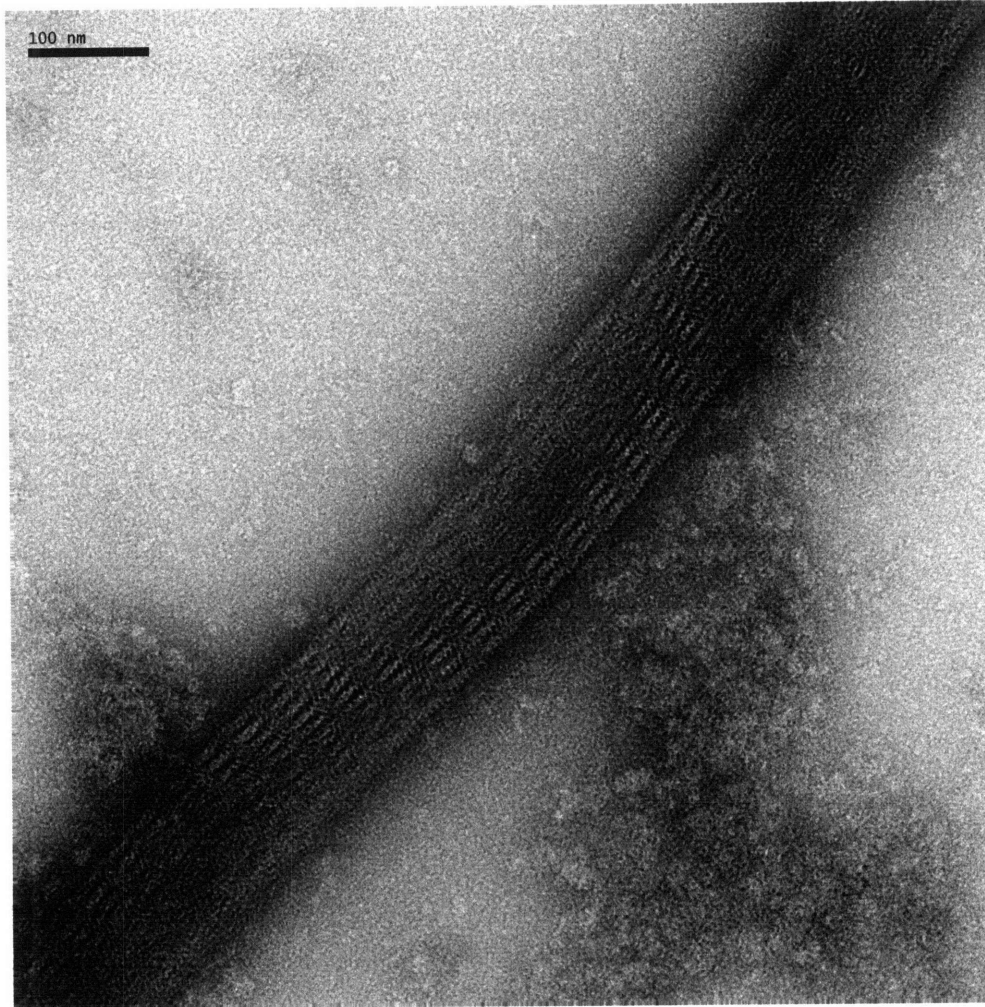
Figure 2-13: Straightened FD Bundle. The EM image shows a periodic crystalline structure throughout the 1 micron segment. The order seems to run in a right-handed fashion and with a 700 nm period, contrary to native FD structure.

Chapter 3

Techniques of Rheology on Methyl Cellulose

We report on rheological measurements of methyl cellulose solutions using several different techniques. Methyl cellulose is of interest to the biological sciences for its role as a viscosity-enhancing agent. Our investigations of this polymer are the first to probe and compare the viscosity of methyl cellulose solutions using four rheometric methods. We distinguish between macro- and microviscosity in these experiments, as there is significant difference depending on the length scale probed. To measure macroscopic viscosity, we use a rheometer in steady shear and small amplitude oscillatory shear modes. To measure microscopic viscosity, we use one-point multi-particle tracking of beads. We also trap a bead with laser tweezers and move the stage to effectively drag a bead through the methyl cellulose solutions, thereby determining the viscosity of the solutions. We observe over an order of magnitude difference in viscosity depending on which length scale is being probed. The Cox-Merz rule holds in microrheological measurements for high concentrations as it does in macrorheological measurements.

3.1 Rheology

Complex fluids (or non-Newtonian fluids) exhibit a significant range of physical characteristics beyond the simple viscous behavior of classical Newtonian fluids. Two of the most fundamental characteristics used to describe complex fluids in varying degrees are elasticity and viscosity. Measurement of these viscoelastic properties has traditionally relied on rheometers–instruments which apply linear and oscillatory shear stresses to the fluids and measures the resulting behavior. For linear stresses, one can define a steady-state shear viscosity, $\eta(\dot{\gamma})$, where $\dot{\gamma}$ is the imposed shear rate. The relevant parameter describing the viscoelastic response to an oscillatory shear strain (small-amplitude oscillatory shear or SAOS) of frequency ω is the complex shear modulus, $G^*(\omega)$. The real part of $G^*(\omega)$, $G'(\omega)$, represents the in phase elastic component of the response, and is called the storage modulus. The imaginary part, or loss modulus $G''(\omega)$, represents the out of phase viscous component [38]. A complex viscosity is defined as $\eta' - i\eta'' \equiv \eta^* \equiv G^*(\omega)/i\omega$. Its magnitude is $|G^*|/\omega$.

While rheometers have extraordinarily advanced the field of rheology, a significant drawback is inherent in their design. Current state-of-the-art rheometers are only able to probe behavior on a $\sim$ 10-μm scale, leaving the shorter dimensions unexplored. Such minute scales are important because the molecules constituting the complex fluids are on this scale, and give rise to the behavior observed in macrorheology. Thus, access to the shorter length-scales will contribute to a greater understanding of the behavior of complex fluids in general.

3.2 Microrheology

Recent advances have allowed for the investigation of behavior on a $\leq$ micron scale [39, 40, 41, 42]. Termed microrheology, the technique involves tracking the motion of tracer particles embedded in the fluid of interest. Usually, the particles of interest are nanometer-sized silica or polystyrene beads, and the motion is thermally driven. From such motion (measured by the mean squared displacement as a function of

time, or $\langle \Delta r^2(t) \rangle)$, the linear viscoelastic responses of the fluid can be determined. The phenomenological generalized Stokes-Einstein (GSE) equation

$$\tilde{G}(s) = \frac{k_B T}{\pi a s \langle \Delta \tilde{r}^2(s) \rangle},\qquad (3.1)$$

provides the means to do so [43]. This equation has been transformed from the time domain to the frequency domain using a Laplace transform. To obtain the traditional viscoelastic moduli, G' and G'', the frequency is extended into the complex domain via analytic continuation [42]. Application of the Kramers-Kronig relations to G^* finally results in the relevant moduli [44].

3.3 Cox-Merz Rule

It has been observed that a correspondence occurred between the steady state shear viscosity, $\eta(\dot{\gamma})$ and complex viscosity amplitude ($|\eta^*| = |G^*|/\omega$) [45]. Polymer melts, concentrated, and semi-dilute solutions have all been found to obey this empirical relationship known as the Cox-Merz rule. However, this correspondence has been only probed in the macro-regime. With microrheology, it is possible to probe this relationship on the micro-regime.

Microrheology provides the means to passively probe the dynamics of complex fluids on a micron length-scale [46, 47, 48]. We investigate the Cox-Merz rule using this technique to measure the viscosity of a complex fluid. To make the analogy with steady shear viscosity, we use a laser tweezer apparatus to apply a shear drag force on a bead. Such a technique can be used to investigate the relationship between linear and oscillatory strain in the microrheological domain, as linear and oscillatory strain do in macrorheology.

We use the technique of one- and two-particle microrheology to determine the viscoelastic behavior of one particular polymer relevant to biological studies, methyl-cellulose (MC) and Stokes' drag, ($f_{Stokes} = 6\pi r v \mu$) to find the microscopic equivalent of the steady state shear viscosity. One-point particle tracking has the disadvantage of only sampling the immediate vicinity of a particle (within 1-2 diameters). This aspect

can introduce inaccuracies into the measurement of the moduli, as inhomogeneities in the sample can skew the ensemble average of the mean square displacement. To circumvent this, two-point microrheolgy was used. This method calculates the cross correlelation between the mean square displacement of two particles, and hence yields measurements spanning tens of μm of sample [41].

One use of MC is as a viscous agent, which increases the viscosity of solutions merely by adding the polymer. Quantifying the micro-viscosity of this viscous agent is relevant to studies involving cellular motility [49, 46]. A difference between the micro- and macro-viscosities of MC has been qualitatively observed by Berg [50]. We investigate the behavior of MC, and we find that the Cox-Merz law holds in the micro-regime.

Methods & Materials

Methyl cellulose preparation: We used artificial sea water (ASW: 423 mM NaCl, 9 mM KCl, 9.27 mM CaCl$_2$, 22.94 mM MgCl$_2$, 25.5 mM MgSO$_4$, 2.15 mM NaHCO$_3$, 10 mM Tris, pH adjusted to 7.9-8.0) as the solvent for the methyl cellulose (MC) powder (M0387-100G from Sigma). We made solutions which varied in concentration from 1% to 4% (wt/vol). To completely dissolve the powder in ASW, we heated ASW to $\sim$80°C with a water bath, then added MC under stirring. Solutions were then stored at 4° C.

Macrorheology: We performed all macroscopic measurements using a rheometer (TA Instruments AR2000) outfitted with a 2° cone-and-plate geometry and set to a 50-μm gap. Two methods were used for each MC sample: small amplitude oscillatory shear (SAOS) and shear sweep experiments. All experiments were performed at room temperature.

Multi-particle tracking microrheology: To measure viscosity on a micron length scale we performed multi-particle tracking (MPT) analysis on fluorescent silica beads manually mixed into the MC samples (1:100 dilution). The beads (provided by David Weitz's lab) were 100 nm in diameter and PEG functionalized to avoid any interactions with the polymer and ASW. We sealed the MC between a glass slide and a

Corning #1.5 cover slip using UV-cured silicon adhesive. Bead positions were collected via a frame grabber at 30fps and digitized. Data was analyzed using software developed by Crocker [51].

Stokes' drag viscosity measurements: We mixed silica beads of diameter 490 nm (Bang Labs) to the MC solutions in 1:100 volume dilution and trapped one bead with a laser tweezer setup. The index of refraction of the MC solutions was measured using a refractometer. To probe viscosity, we applied a drag force by moving the stage at set velocities and then measured the equilibrium bead displacement from the center of the trap. Trap strength was determined by measuring the mean square displacement of the bead and using the equipartition theorem.

Trap Instrumentation: The optical tweezers instrument offers high end automated functionality and is based on a customized inverted microscope (Nikon) with a design plan similar to that presented by Lang et al. [52]. The microscope has been heavily modified to increase its mechanical stability and allow for the incorporation of a three-axis piezo-electric translation stage capable of nanometer resolution (Physik Instrumente). This stage can sweep distances at velocities that range from nanometers to millimeters per second and offers a great variety of drag force magnitudes that can be exerted on trapped objects. Optical tweezer capabilities were achieved by focusing a 1064-nm laser (Coherent) to a diffraction limited spot using a 1.40 NA objective lens (Nikon). The position and intensity of the optical tweezers in the specimen plane were precisely controlled with a pair of acousto-optic deflectors (AODs) (IntraAction Corp.) placed along the path of the trapping beam in a position conjugate to the back focal plane of the microscope condenser lens.

The instrument also contains a position detection sub-system based upon a 975-nm detection laser (Corning Lasertron) that is coincident with the trapping laser. After passing through the microscope condenser lens, the detection beam was spectrally isolated and imaged on a quadrant photodiode (QPD) (UDT Sensors) for back focal plane detection [53]. Signals from the QPD were acquired using a 16 bit A/D board (National Instruments) and the relative displacements of trapped microspheres were easily resolved at the nanometer level. Position calibrations were performed for

all trapped beads by using the AODs to raster scan them relative to the detection laser while sampling scatter distributions using the QPD as previously described [52]. Custom software (LabView, National Instruments) was used to acquire data at rates of 100 kHz and to control and automate all instrument components throughout the experimental procedures. The stiffness of the trap was determined by monitoring the thermal fluctuations of a trapped bead for several seconds and applying the equipartition theorem for every degree of freedom in the system: $k \langle x^2 \rangle = k_B T$ where k_B is Boltzmann's constant, T the absolute temperate of the system, $\langle x^2 \rangle$ the mean square displacement of the bead from its equilibrium position in a given axis, and k the stiffness of the trap in that axis. This calibration method was chosen because it does not require a priori knowledge of the viscosity of the fluid in which the beads are suspended, which is an unknown in these experiments. The viscosity of the medium can be determined by moving the piezo-electric stage at a constant speed and measuring the position of the trapped bead. At equilibrium, the force imparted on the bead by the optical trap equals the force originating from viscous (Stoke's) drag. This allows for a simple expression for viscosity of the system:

$$\eta = \frac{0.86kx}{6\pi r v} \tag{3.2}$$

where x is the change in position of the trapped bead in a given axis, v the speed of the fluid relative to the bead, and r the radius of the bead. Note that the 0.86 factor in the above expression accounts for the increase in hydrodynamic drag resulting from the interaction of a sphere with a boundary layer of water close to a surface (Faxen's law). This factor was estimated from Faxen's law for a bead with a radius of 245 nm being dragged at a height above the surface of approximately 1000 nm [54].

Results & Discussion

To ascertain the validity of the Stokes' drag method, we first measure the viscosity of DI water as a calibration. We obtain a value of 0.0011 ± 0.0002 Pa·s, consistent with measured values for water (Figure 3-2). We also investigate the trap stiffness as

48
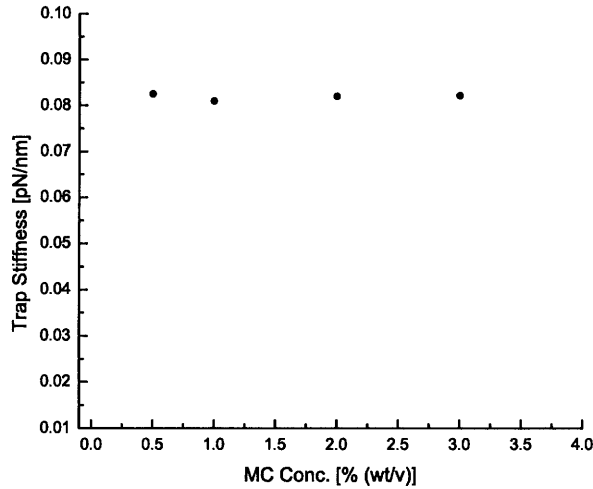
Figure 3-1: Trap Stiffnesses of Varying MC Concentration Solutions. No dependence of trap stiffness on MC concentration is observed.

a function of MC concentration and find that there is no dependence (Figure 3-1). Since the trap stiffness is only a function of the mismatch in refractive index of the bead and solution, we measured the indices for the MC solutions and found that they varied only slightly from that of water ($\leq$ 1%), indicating that the measurements from Figure 3-1 are consistent.

We report first on macroscopic viscosity measurements for MC to verify that the Cox-Merz rule holds for MC macroscopically. We perform small-amplitude oscillatory shear (SAOS) tests on the MC solutions to find G' and G''. We perform also shear sweep experiments, measuring viscosity directly. The dynamic range explored in shear sweep measurements is $\sim 10^{-1}$ to 10^2 s^{-1}. For SAOS measurements, we probe between frequencies of an equivalent dynamic range. We find that the CM rule holds for higher concentrations and high shear rates (Figure 3-3).

The divergence between shear viscosity and complex viscosity at low rates is due to MC having a yield stress. Materials with a yield stress behave as a solid at low oscillation frequencies. Moreover, the Cox-Merz viscosity curve, $|\eta^*| = |G^*|/\omega$, diverges with a -1 power dependence as $\omega \rightarrow 0$. This follows because G' and G'''

49
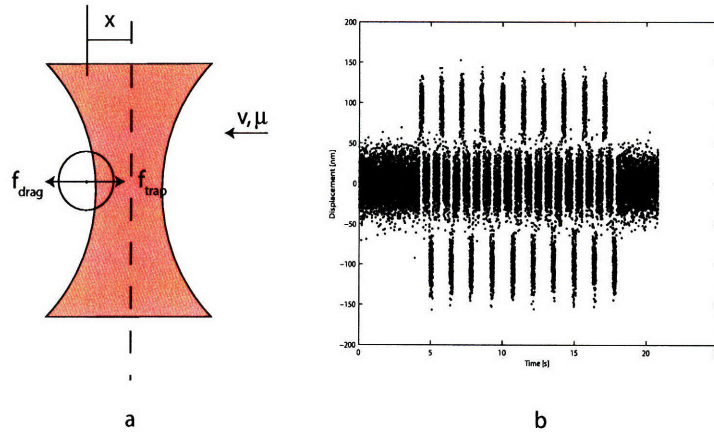
Figure 3-2: Measuring Viscosity of Water Using Stokes' Drag. a. The bead position relative to the center of the trap during Stokes' drag experiments measuring the viscosity of water. The bead is displace from the trap center because the stage is moved at a constant velocity to induce the Stokes' drag. b. A Displacement vs. Time graph from one experiment measuring the viscosity of water.

approach non-zero finite values for materials with yield stress behavior. This behavior manifests as a curve with a slope of -1 in a log-log plot, which we observer for our solutions.

For MPT, we have data for 1-4% MC, see Figure 3-3. We record motion for three minutes, then digitize the footage and calculate G' and G''. We perform both one- and two-point multiple-particle tracking analysis to obtain the microrheological behavior (Figure 3-4).

We see that that the one- and two-point measurements agree. This indicates that the MC is homogeneous from $\sim 0.1 - 100 \mu m$. We have also performed measurements using 2-μm diameter beads which have given similar results to Figure 3-4. With the one- and two-point MSD in agreement, we are confident that there are no inhomogeneities within the sample affecting our measurements. The persistence length of MC has been measured using light scattering and small angle x-ray scattering to be ~ 20 nm, so no caging artifacts arise [55].

From the above measurements, we find that the Cox-Merz rule holds to almost exactly for the macrorheology, and reasonably well (to within half an order of magnitude) for the microrheological measurements. Such a correspondence on the

50
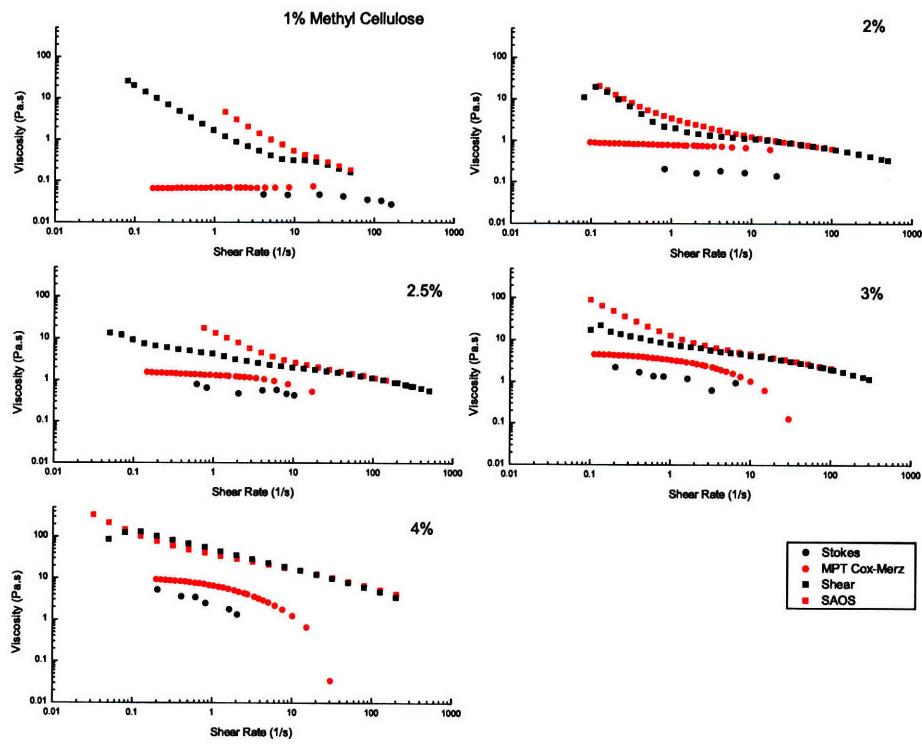
Figure 3-3: Methyl Cellulose Viscosity Comparison. Comparisons of viscosity measurements from all technqiues.
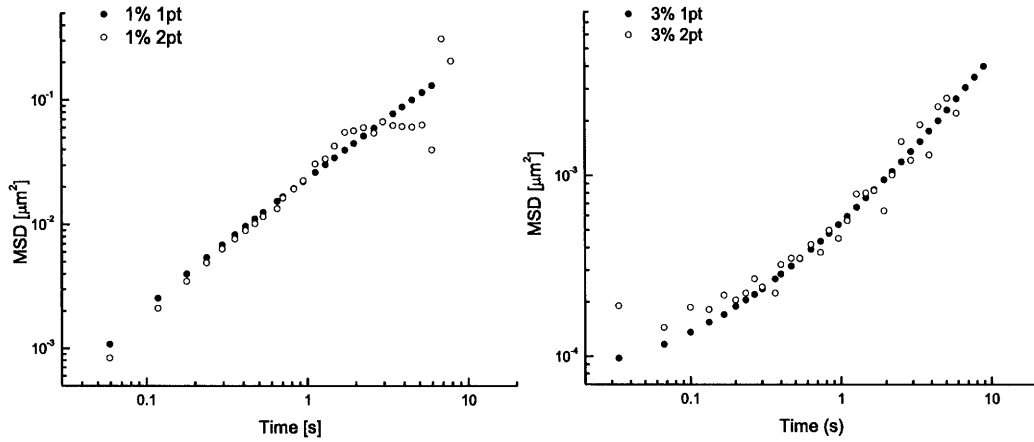
Figure 3-4: One- and Two-Point Microrheology. One- and two-point MSD measurements using 100-nm diameter beads in 1% and 3% MC solutions. The two curves yield a close match, which indicates that the samples exhibit no inhomogeneities.

macro-scale is expected. However, the correspondence between microrheology and our Stokes' drag experiment has not been reported, and suggests that the origins of this empirical relation lie within a microscopic mechanism.

Though there is agreement between the linear and oscillatory results, the disparity between measurements of the macro-viscosity and micro-viscosity suggest that a mechanism increases the measured viscosity on a macro-scale which is not observed on the microrheological measurements. Since MC is an entangled network with no crosslinking, coil-coil interactions may account for the additional viscosity. Recently, workers have used the tube model of Doi and Edwards to understand the relationship, resulting in relations which fit our microscopic results [56].

Chapter 4

Force of An Actin Spring[1]

Cellular movements are produced by forces. Typically, cytoskeletal proteins such as microtubules and actin filaments generate forces via polymerization or in conjunction with molecular motors. However, the fertilization of a *Limulus* egg involves a third type of actin-based cellular engine-a biological spring. During the acrosome reaction, a 60-μm long coiled and twisted bundle of actin filaments straightens and extends from a sperm cell, penetrating the vitelline layer surrounding the egg. A subtle overtwist of 0.2°/subunit underlies the mechanochemical basis for the extension of this actin spring. Upon calcium activation, this conformational strain energy is converted to mechanical work, generating the force required to extend the bundle through the vitelline layer. In this paper, we stall the extension of the acrosome bundle in agarose gels of different concentrations. From the stall forces, we estimate a maximum force of 2 nN and a puncturing pressure of 1.6 MPa. We show the maximum force of extension is three times larger than the force required to puncture the vitelline layer. Thus, the elastic strain energy stored in the acrosome bundle is more than sufficient to power the acrosome reaction through the egg envelope.

---

[1]This chapter has been published as [57].

4.1 Cellular Forces

Cellular engines at the molecular level typically generate pN levels of force and nm-scale movements. For example, a molecular motor such as myosin produces about 3 pN of force from an ATP-coupled conformational change in the head and neck domains to step along an actin filament in nanometer increments [58, 59, 60, 6]. Polymers such as actin and tubulin generate pN forces as a subunit adds to the end of a filament or tubule [61]. Assembly into macromolecular complexes multiplies the forces generated by each protein. The μN of force generated by a muscle myofibril is the product of individual myosin molecules arranged in parallel and in series with a lattice of actin filaments [62]. Protrusion of the cell membrane results from extension at the free ends of a network of branched and cross-linked actin filaments [63]. Thus typical cellular engines integrate motors or single filament polymerization into a larger structure to generate nN-scale forces required for μm-scale cellular movements [64].

The acrosome reaction in sperm cells of horseshoe crab *Limulus* provides a spectacular example of non-traditional actin motility. To initiate fertilization, *Limulus* sperm cells must penetrate two layers surrounding the egg, an outer basement lamella $\sim$ 5-μm thick and an inner vitelline envelope $\sim$ 35-μm thick. Sperm cells penetrate this physical barrier by uncoiling and extending a 60-μm long bundle of actin (Figure 4-1a) [9]. Structural analysis reveals that, before reacting, the acrosome bundle consists of a para-crystalline array of bent, twisted actin filaments bound to two proteins, scruin and calmodulin. This bundle is wrapped around the base of the nucleus in a helical coil [7].

In the presence of Ca^{++}, scruin changes conformation [18], causing the individual actin filaments to untwist and extend to a homogeneous, straightened bundle called the true discharge (TD) (10). This motility does not involve ATP hydrolysis or a myosin motor protein [7, 31]. Using electron micrographs of the actin bundle before and after activation, DeRosier and Tilney suggested that the force underlying this motility is a spring-based mechanism in which mechanical energy is stored in slight but concerted over-twists of the actin filaments in the bundle, and our quantitative
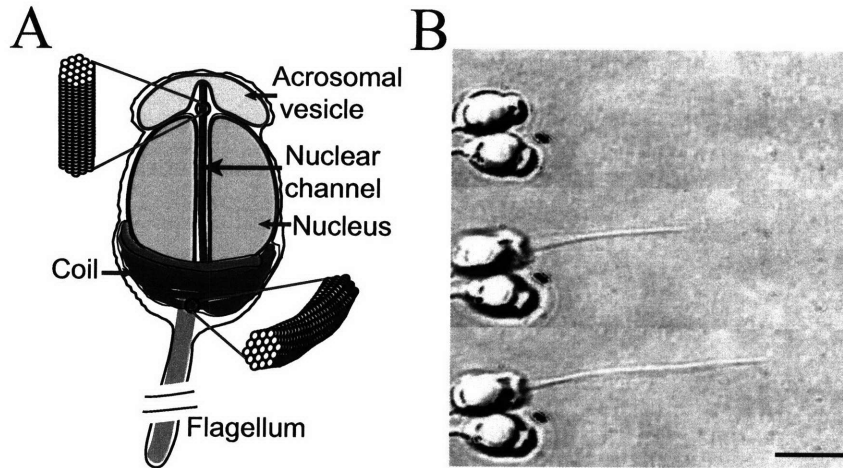
Figure 4-1: (A) A schematic of an un-reacted sperm cell inspired from electron micrographs, showing the proximal end of the acrosome bundle lying in the nuclear channel while the rest of the bundle is coiled around the base of nucleus. (Insets) The filaments are twisted in the coiled state, but parallel to each other in the true-discharge (TD) state. (B) Upon laser activation, a sperm cell embedded in agarose extends the acrosome bundle to a final length of ~15 μm; normally, the cell extends the bundle to a length of 50-60 μm in artificial sea water (scale bar = 5 μm).

experiments confirm this hypothesis [22, 11, 12]. Thus the *Limulus* sperm acrosome bundle is an example of a third type of actin-based cellular engine–a mechanochemical spring where the relevant displacement governing force generation arises from an overtwist rather than from a rectilinear extension or compression from equilibrium.

4.2 Stalling the True Discharge

In this work, we measure and report the maximum force generated by the *Limulus* acrosome reaction. First, we embed sperm cells in a solid block of agarose and trigger the cells to extend the acrosome bundle through a solid block of agarose. During the extension, the acrosome bundle moves against a shear drag exerted by the agarose, and the reaction stalls when the opposing force exceeds the force produced by the acrosome reaction. The stall force is calculated from measurements of the stalled bundle lengths at various agarose concentrations together with stress values from penetration tests of agarose. To corroborate our measurements, we also use

methylcellulose (MC) as a viscoelastic thickening agent to mechanically slow down the extension rate of the acrosome bundle. This method yields a lower bound estimate of the acrosome reaction force, providing an independent verification of our measured stall force. Our work provides the first estimate of the force associated with the mechanochemical conformation change in a bundle of actin.

Methods & Materials

Reaction medium: For the agarose experiments, 0.5% (w/v), 1.0%, 1.5%, 2%, 2.5%, and 3% agarose gels are prepared by mixing low-melting-point (LMP) agarose powder (gel point: 29°C) in artificial seawater (ASW: 423 mM NaCl, 9 mM KCl, 9.27 mM $CaCl_2$, 22.94 mM $MgCl_2$, 25.5 mM $MgSO_4$, 2.15 mM $NaHCO_3$, 10 mM Tris, pH adjusted to 7.9-8.0). The mixture of agarose powder and ASW is heated to $\sim 80°$ C with gentle stirring using a magnetic stir bar until the agarose is completely dissolved. The solution is left to solidify at room temperature (25° C) until the cooled agarose gel becomes translucent. Since the agarose solution exhibits a hysteresis between its melting point ($\geq 50°$ C) and gel point (29° C), the prepared agarose block is re-melted at 65-70°C for 10 minutes and stored in aliquots at 4° C for acrosome reaction experiments and characterization experiments.

Embedding sperm cells in agarose: Horseshoe crab (*Limulus polyphemus*) sperm (500 μl) is collected from a healthy male and stored on ice. The collected sperm are washed at least twice in ASW by centrifugation at 750 g for 5 min. Washed sperm cells are diluted 1:2000 in ASW, injected into a flow chamber that is pre-treated with a tissue adhesive, BIOBOND (Cat# 71304, EMS, Inc, Fort Washington, PA), and incubated for 10-20 min for cells to securely adhere to the bottom of the flow chamber. The sperm-containing flow cell is warmed to $\sim 30°$ C on a heating block and the pre-cooled molten agarose (32° C) is injected into the chamber, completely replacing the ASW. The agarose-filled flow chamber is rapidly cooled to 4° C. Analyses by electron microscopy indicated that the rapidly cooled gels have a homogeneous pore structure [65]. The LMP agarose is ideally suited for our experiments as sperm cells are viable

up to about 40° C.

Inducing the acrosome reaction: All microscopy work was performed on a Nikon TE2000 Inverted microscope with DIC optics and an oil immersion objective. Images were captured with a Sony S-VHS video recorder and digitized to a PC for analysis. Typically, the acrosome reaction in the *Limulus* sperm, as well as in other marine invertebrate sperm, is triggered by flowing calcium ionophore which transports extracellular Ca^{++} into the cytoplasm. Our recent finding has shown that a focused 488-nm laser can also induce the acrosome reaction when it is used to irradiate certain regions of the sperm cell. For efficient triggering, we focus the beam to a diffraction-limited spot using a 100X 1.4 N.A. microscope objective lens. Measured immediately before entering the objective lens, the beam intensity is $\sim$ 7 mW. Compared to the traditional use of calcium ionophore for activation, our newly discovered laser irradiation allows us to trigger the acrosome reaction on selected cells on demand, and even on cells embedded in solid media.

Characterizing agarose: We perform penetration tests with a Materials Testing Machine (Zwick TC-FR010TH Allround-Line) to characterize the shear and crack opening stresses agarose exerts on the extending acrosome bundle. We operate the instrument in a compression mode, moving the probe at a fixed velocity. The probe is mounted on a load cell (Zwick KAP-TC 10N), a device which converts mechanical force into an electrical signal. This load cell monitors the amount of force exerted during compression to maintain a fixed velocity as the probe is moved through the agarose block.

In this study, we assume that the agarose is a homogeneous continuous medium. For such an ideal solid, the shear stress along the probe is independent of the probe diameter and thus the frictional force that resists the motion of the probe simply scales with the diameter of the probe. Furthermore, the stress is not a function of the travelling velocity of the probe. To a first approximation, it is reasonable also to assume that surface interaction of agarose with a metal probe is similar to that

of the actin bundle and agarose, for both the metal probe and bundle are crystalline structures.

We choose a stainless steel probe of $R_{rod} = 0.54$ mm with a tapering tip, and set the probe velocity to 1.0 mm/s so that the normalized velocity $\bar{v} = v/R_{rod} \sim 2$ s^{-1}, corresponds to the acrosome reaction velocity of 0.1 m/s for the bundle of 50-nm tip diameter. As shown in Figure 4-2b, the probe is set to penetrate and puncture through an agarose block of thickness δ. We measured the distance travelled by the rod through the agarose as a varying force is applied to maintain a pre-set velocity. The force-displacement curve consists of distinct transient (I) and steady state (II) regimes (Figure 4-2c). While penetrating through the block, the force exerted by the load cell is opposed by two forces, namely the crack opening force associated with the development of a crack in front of the extending tip, F_{crack}, and the frictional shear force along the surface of the probe, F_{drag}. We treat these two forces as additive so that $F_{total} = F_{crack} + F_{drag}$. Once the rod punctures through the slab, it reaches a steady state where only the frictional force opposes the motion, since there is no longer agarose in front of the tip. From the steady state force, F_{ss}, we calculate the steady state shear stress from the frictional drag along the bundle, $\tau = F_{ss}/2\pi R_{rod}$, where δ is the total thickness of the agarose block. The crack opening force is then calculated by subtracting the frictional drag force from the total force, $F_1, F_2, F_3, \ldots, F_n$, in the transient regime (I) as in $F_{crack} = F_n - F_{ss} = F_n - \tau 2\pi R_{rod}(d_n - d_0)$. We repeat the experiments while varying the diameter of the probes and the penetration velocities to verify that the effects of these parameters in the stress measurements are not significant.

Characterizing methyl cellulose: We use MC solution to mechanically slow down the acrosome reaction. To determine the viscosity of MC solution, we apply a Stokes' drag force to a laser-trapped 0.5-μm diameter glass bead in MC solutions. This method probes a length-scale comparable to that of the bundle diameter, a factor not shared by more conventional rheology methods. We trap the bead with the laser trap, then move the stage, and thus MC solution, at a controlled velocity. The moving fluid

induces a drag force on the bead and displaces it from the center of the trap. The trap behaves like a spring, exerting a linear restoring force $F_{trap} = -kx$ on the bead. The distance, x, is measure from the center of the trap, and the spring constant, k, is found via the equipartition theorem $k \langle x^2 \rangle = k_B T$ with one degree of freedom. By balancing Stokes' drag with the linear restoring force of the trap, we find the viscosity of the solution.

Results & Discussion

When activated in ASW, a 60-μm long actin bundle extends from the cell in 15 s. However, in agarose, the bundle extends at a much slower rate and stalls before full extension. This occurs because the bundle is opposed by two forces. While tunneling through the block, the total force opposing the bundle motion is the sum of two linear forces, a macroscopic shear stress and a crack opening stress. As a result of this total force, the acrosome extension in agarose is stalled at a shortened length.

To quantify the force exerted during the TD reaction, we balance the forces in the acrosome bundle-agarose system (Figure 4-2a). Because a 1.5% agarose block has an average pore size of 150 nm and higher concentrations only reduce the pore sizes [66], we treat agarose as a homogenous continuous solid. Doing so on the bundle at the moment it stalls $x = L_s$, yields an expression for the acrosome stalling force F_s:

$$F_s = F_{crack} + F_{drag} = \sigma_c \pi R_a^2 + \tau 2 \pi R_a L_s \tag{4.1}$$

Here is the acrosome bundle radius, the first term is the force required to open a crack and the second is the frictional force associated with moving the bundle relative to the agarose, where τ is the shear stress, and σ_c the crack opening stress associated with the penetration of the agar by the actin bundle. To determine the shear stress, τ, and crack opening stress, σ_c, we carry out penetration tests on agarose using needles of various diameters. The shear stress, τ, measured at steady state exhibits gradual increase with agarose concentration. The crack opening stress, σ_c, shows a minor increase from 2% (w/v) to 2.5% agarose, but it almost doubles from 2% to 3% agarose. Because both crack opening and shear stresses increase at higher concentrations of
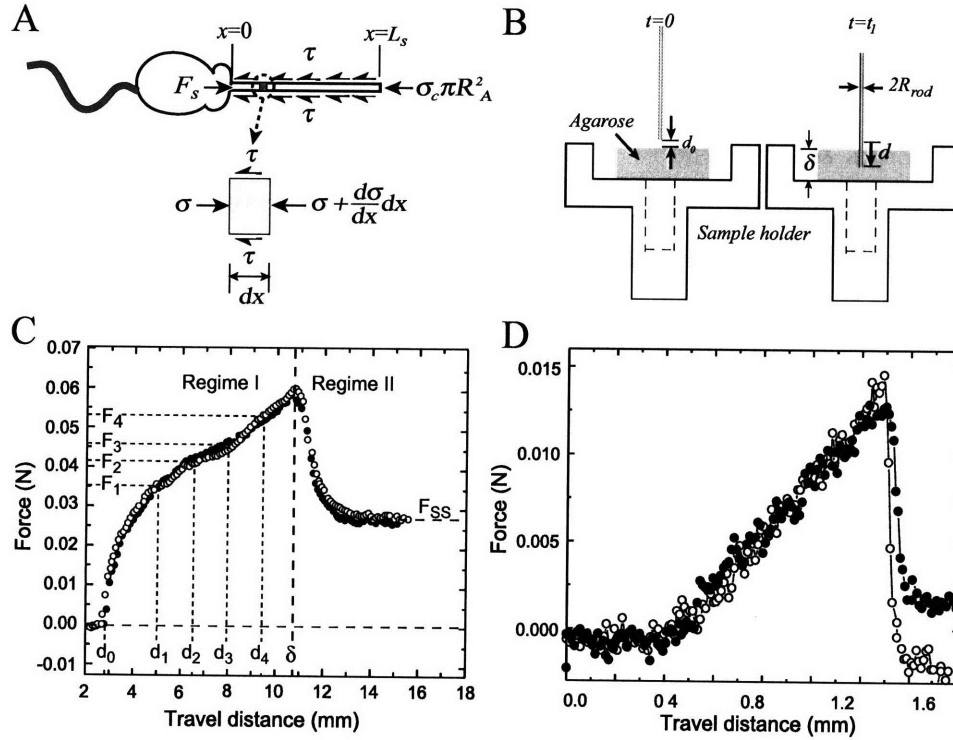
Figure 4-2: Analysis to determine forces opposing acrosome bundle extension. a. Forces acting on the extending acrosome bundle. When the embedded cells react, the extending acrosome bundle inside the agarose is opposed by both a frictional force, F_{drag}, along the bundle and a crack opening force F_{crack} at the tip. We balance forces on a differential element of the bundle at the moment it stalls, $x = L_s$, to estimate F_s. b. A specimen holder has a through-hole in the middle so that the probe can puncture through the slab of agarose gel. c. Force vs. travel distance of the probe ($R_{rod} = 0.54$ mm) as it penetrates through a slab of 3% agarose. The probe makes initial contact with the gel when $d = d_0$ and penetrates through when $d = \delta$. In the transient region I, both frictional drag and crack opening force oppose the penetrating probe while only frictional drag exists in the steady state regime II. d. Force vs. travel distance from the puncture test on *Limulus* eggs using 100-μm radius platinum wire.

60

agarose (Figure 4-3c), the stall length of the acrosome bundle shortens (Figure 4-3b). Figure 4-3c shows the magnitudes of the shearing drag stress and crack opening stress measured with a stainless steel probe of $R_{rod} = 0.54$ mm at a probe velocity of 1.0 mm/s. The dominant component of the total force is frictional drag, since the crack opening force contributes less than 10% to the total. Using estimates of the shear stress τ, the crack opening stress σ_c, and the stall lengths L_s at various agarose concentrations, we obtain the acrosome reaction force at the moment of stalling using Equation 4.1 (Figure 4-3d). Averaging the results from our calculations, we arrive at an acrosome stalling force of $F_s \sim 1.9$ nN (Figure 4-3d).

We also consider the shear stress dependence on the probe geometry and the velocity. With macroscopic probes, we observe that, for 3% agarose, the shear stress weakly increases with decreasing probe diameter and increasing probe velocity. These measurements indicate that agarose mildly deviates from an ideal continuous medium, but the magnitudes of these trends are small and do not affect our force calculation significantly.

As an independent means to verifying these measurements, we used a solution of methyl cellulose (MC) and ASW in order to mechanically slow down the extension rate of the acrosome bundle. Unlike the experiments with agarose, the acrosome bundle is able to extend to its full length with a finite final velocity. For the acrosome bundle to extend in a viscous medium at a finite velocity, the force generated by the acrosome reaction must at all times exceed the opposing viscous drag, and thus the maximum drag force exerted by the environment yields a lower bound of the acrosome reaction force. For a viscoelastic fluid, the drag force F_V can be found by using the Stokes equation for a cylinder only in the limiting case of viscous regime with Deborah number (De)$\ll$1 [67]:

$$F_V \sim \frac{2\pi\mu_m x v}{\ln\left(\frac{x}{2R_a}\right) - 0.2}, \tag{4.2}$$

where μ_m is the viscosity of the MC solution, x is the length of the extended bundle, and v is the velocity of the extension at the length x. An MC solution of 4% (wt/vol)

or lower exhibits a Newtonian viscous liquid-like behavior with De≪1 while one 5% or above behaves more like an elastic solid. We obtain a maximum lower bound force using the viscosity from the 4% MC solution. For a strain rate of 0.2 s^{-1}, which is the characteristic strain rate for the extending acrosome bundle in the 4% MC solution, the viscosity is measured to be $\sim$ 5 Pa·s. Using Equation 5.1, the average force values at 4% MC is calculated to be $F_{low} \sim$ 260 pN, and provides a lower bound estimate for the force of the acrosome reaction. This is about a seventh of the upper bound force obtained from stalling experiments, further substantiating the validity of our force estimates.

To determine whether the mechanical force of the acrosome reaction is sufficient to puncture an egg surface, we measure the force required to puncture the vitelline layer of the *Limulus* egg (diameter$\sim$2 mm) using a 100-μm diameter platinum wire to push against the egg (Figure 4-2d). The puncturing pressure is calculated as $P_F = F_{max}/R_{rod}^2$ and the average value from 8 different eggs is 0.45±0.06 MPa. Based on our stalling force measurements, $F_s \sim$ 1.9 nN, the imposed pressure on the egg by the tip of the acrosome bundle is $\sim$ 1.56 MPa. Thus, the coiled actin bundle generates approximately three times the stress necessary to mechanically puncture the egg vitelline layer. In terms of the stall force, we can also estimate the amount of energy released during the reaction. Since the stall force is the maximum force the acrosome reaction can generate, the total energy dissipated over the average stalled length of $l \sim$7 μm at 3% agarose is calculated to be, at most, $W = \tau R l^2 \sim$1.58×10^{-14} J. For comparison, the stored elastic energy of the 7-μm section of the bundle is 3.5×10^{-14} J, based on our earlier measurements of the twist strain and the twisting stiffness of the bundle [31, 11]. Thus the stored elastic energy associated with the overtwist of the actin filaments is fully capable of providing all the energy required to power the extension and provide a force to penetrate the vitelline layer. To compare with other modalities of actin-based cell motility, it is useful to view the dynamics of this spring in terms of a specific power. The entire bundle consists of roughly 1.1 million subunits of the actin-scruin-calmodulin complex and its total mass is 3.1×10^{-16} kg. Using a typical velocity of 10 μm/s and a stalling force of 1.9 nN yields a value of
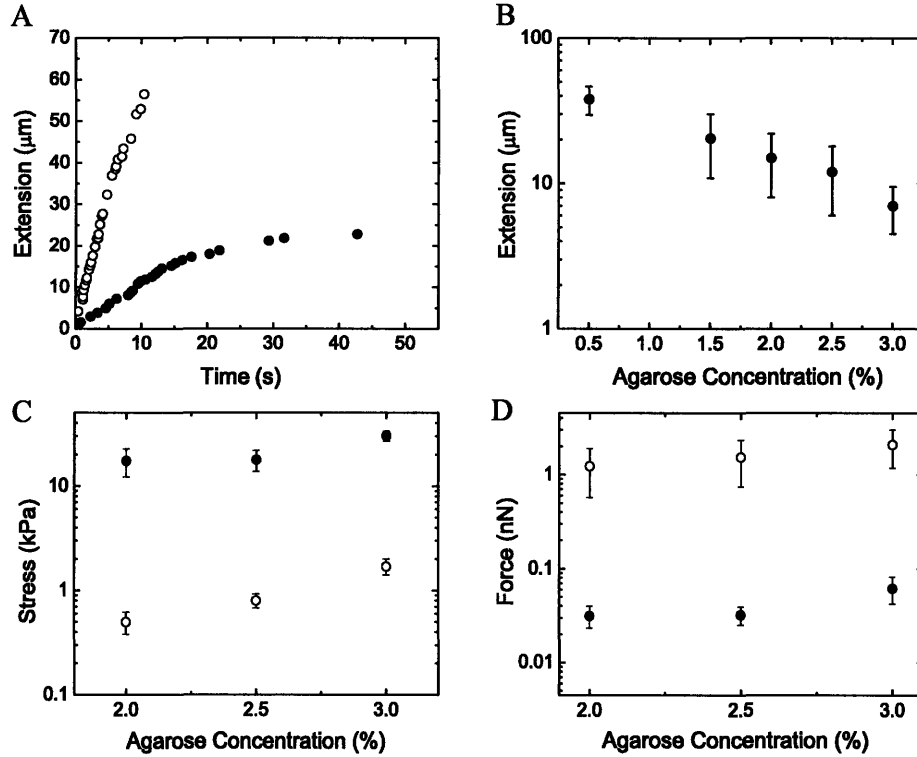
Figure 4-3: Stalling the True Discharge. a. Graph shows typical extension for a sperm cell in sea water (open circle), and a cell in 2% agarose (solid circle). Note the cell in agarose stalls at 20 μm. b. Stall lengths of the acrosome bundle decrease as agarose concentration increases. c. Agarose characterization results for a stainless steel needle of $R_{rod} = 0.54$ mm. Stress vs. agarose concentrations. Solid circles are crack opening stress values, and open circles represent the shear stress. d. Shear (open circles) and crack opening (solid circles) forces exerted on acrosome bundle. Total acrosome force at the moment of stalling is found by summing both crack opening and shear drag forces, $F_s = F_{crack} + F_{drag}$. We have consistent values of the total stalling force at all concentrations of agarose, with an average F_s ~1.9 nN.

65 W/kg for the specific power of the actin spring. Recent measurements report the force generated by the actin polymerization motor to be ~ 2 nN per μm of the margin of the leading edge of a lamellipodium [5]. For a typical leading edge of volume, the mass of actin monomers participating in the polymerization motor is estimated to be 1.8×10^{-15} kg. With a velocity for filamentous actin of 0.26 μm/s, we obtain a specific power of 13 W/kg for the polymerization motor. At a cellular level, the simple mechanochemical spring represents a powerful engine and its specific power is almost 5 times larger than that of a lamellipodium.

For the sperm cells of marine invertebrates such as the horseshoe crab, the vitelline layer of the egg presents a formidable physical barrier to fertilization. The solution to this biological problem lies in a chemically triggered version of a simple engineering device—a spring. We have quantified the ability of this actin spring to store and release elastic energy, and to mechanically produce force and motion. From these purely conformational changes, the sperm cell is able to puncture the protective layers of the egg and achieve fertilization.

Chapter 5

The Role of Calcium

We investigate the role of calcium during the acrosomal reaction, or true discharge (TD), of *Limulus* sperm cells. By irradiating a section of the flagella with a focused green laser, we induce the TD singly in individual cells. This technique allows us to analyze the dynamics of extension as a function of external calcium concentration. We show that extension requires the continuous presence of external calcium, and that varying this concentration affects the extension dynamics. Though the extension length displays nonlinear behavior in time, we find that the volume of the extended bundle as a function of time is linear. These results suggest that the acrosome extension is a local phenomenon, and that the extension is consistent with a sequential, constant rate calcium-calmodulin binding mechanism.

5.1 Calcium Regulation

Calcium is essential for many biological processes involved in cellular motility. Muscles contract because of a conformational change experienced due to calcium binding to the protein troponin C [68]. Calcium is also involved in mitosis where centrin, another Ca^{++}-sensitive protein, is found to be a component in the centrosome [69]. Another cellular system involving calcium regulation and motility is the contraction of the unicellular organism, *Vorticella* [70]. In each of these systems, calcium emerges as a key participant in processes vital to living systems. In this paper, we describe our work

involving calcium regulation during the initial stages of horseshoe crab fertilization.

In vitro initiation of the reaction can be achieved by two different methods. The first uses a calcium ionophore to deliver external calcium ions into the cell. A second method triggers the TD by using a diffraction-limited laser beam to irradiate a region of the cell. Though the presence of external calcium is required for the reaction to occur, no further experiments have been conducted to investigate the role calcium plays in the reaction. It has been postulated that calcium is only required to initiate the reaction, and that subsequent extension proceeds independently of calcium.

In this series of experiments, we investigate the role calcium plays in the acrosome reaction. By controlling the presence and concentration of external calcium, we are able to control the activation as well as speed of the reaction. We detail a quantitative model of the extension consistent with observations. Our model accommodates a sequential calmodulin-calcium binding mechanism and presents a natural region within the bundle wherein the reaction occurs. From our experiments and our model, we are able to calculate in vivo rate constants for CaM-Ca^{++} binding which are comparable rate constants observed in other calcium binding systems [71, 72].

Methods & Materials

Sperm cells were collected from male crabs and washed in artificial sea water (ASW: 423 mM NaCl, 9 mM KCl, 9.27 mM CaCl$_2$, 22.94 mM MgCl$_2$, 25.5 mM MgSO$_4$, 2.15 mM NaHCO$_3$, 10 mM Tris, pH adjusted to 7.9-8.0) twice. The sample was then diluted 1:1000 with ASW and flow the solution of cells into a flow chambers constructed from cover slips and double-sided adhesive tape to conduct the experiments. To immobilize the cells, the bottom cover slip was first treated with a 2% (v/v in acetone) BIOBOND non-specific adhesive solution and then rinsed with water.

An EGTA solution was made by substituting 0.1 mM EGTA for 9.27 mM CaCl$_2$ to chelate residual Ca^{++} ions. This zero-Ca^{++} solution was added to the flow chamber. Solutions for the calcium titration experiments were made by dissolving additional amounts of CaCl$_2$ to ASW as required to achieve desired calcium concentrations.

All experiments were performed at 25° C. To image experiments, a Nikon TE-

2000 inverted microscope with a NA 1.4 100X oil-immersion objective was used. A laser tweezer-like setup was installed with a 532-nm 25mW laser from World Star Tech (Toronto, Canada). Video was recorded with a Dage MTI CCD100 camera, and digitized for tracking with a PC. Individual extension profiles were visually tracked using software provided by Photron Cameras (San Diego, CA, USA). All experiments were performed at room temperature.

Results

Our first set of experiments involves using EGTA to completely eliminate the presence of external calcium during the reaction. Initially, we trigger the TD reaction and monitor the extension. While the actin bundle is extending, we flow in a solution of zero-Ca^{++} ASW with 0.1mM EGTA, completely eliminating calcium. This has the effect of arresting all motion within a second. Re-introducing normal ASW to the flow chamber 30 s later results in a resumption of the extension, though with a lower velocity. Figure 5-1a shows the extension profiles for five individual cells representative of the phenomenon. We note that the extension rate after the arrest is significantly smaller than before.
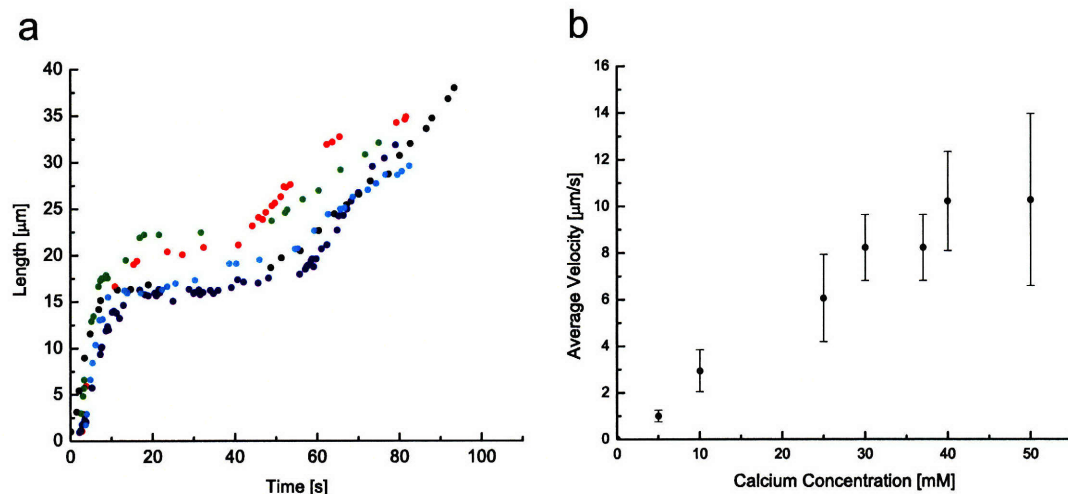

Figure 5-1: Effect of Calcium on TD Extension. a. In the absence of external calcium, the acrosome reaction is arrested. Re-introducing calcium restarts the extension. Each color represents a single cell. b. The average velocity of the TD extension increases at higher calcium concentrations.

A second series of experiments reverses the order of solutions added. Instead of ASW, we initially exposed the cells to the zero-Ca^{++} ASW solution and then trigger the TD. In none of these experiments did the laser irradiation trigger the TD. However, by replacing the zero-Ca^{++} solution with ASW within 15-20 s of laser irradiation, we were able to recover the TD extension. Re-introducing ASW after a period greater than 15-20 s did not produce TD extension.

We then investigate the effect various concentrations of external calcium had on the dynamics of extension. To do so, we used ASW with total calcium concentrations of 5, 9 (ASW), 25, 37, 40 and 50 mM. We trigger the acrosome reaction in a solution with a given calcium concentration and track the extension visually. We collect 6-10 sample extension profiles at each concentration. Two observations can be made from these results. First, the average velocity of the extensions increases as a function of calcium concentration, as seen in Figure 5-1b. Secondly, the trajectories of all extensions exhibit significant nonlinear behavior (Figure 5-2).

Discussion

Previous work had established that the TD reaction could only be initiated in the presence of external calcium. No investigation was made into calcium requirements during the reaction. Our study seeks to address this issue in addition to probing the effects external calcium has on the dynamics of the TD extension. To do so, we use laser irradiation to trigger the TD reaction in a controlled environment.

The experiments involving EGTA prove that external calcium must continuously be present for the extension to occur. Explanations of the extension which rely on global 'all-or-nothing' mechanisms such as crack propagation are thus ruled out. A scenario where Ca^{++} only initially triggers the extension, which then proceeds in a self-sustained manner, cannot occur. Such a mechanism would imply that the extension, once initiated, would proceed even in the absence of external calcium. To the contrary, we have shown that the TD reaction proceeds only while the cell is in calcium-rich ASW. Once we flow into the chamber an EGTA-solution, thereby eliminating all traces of calcium, we completely arrest the extension. Moreover, that subsequent extension is observed when calcium-rich ASW is re-introduced suggests a
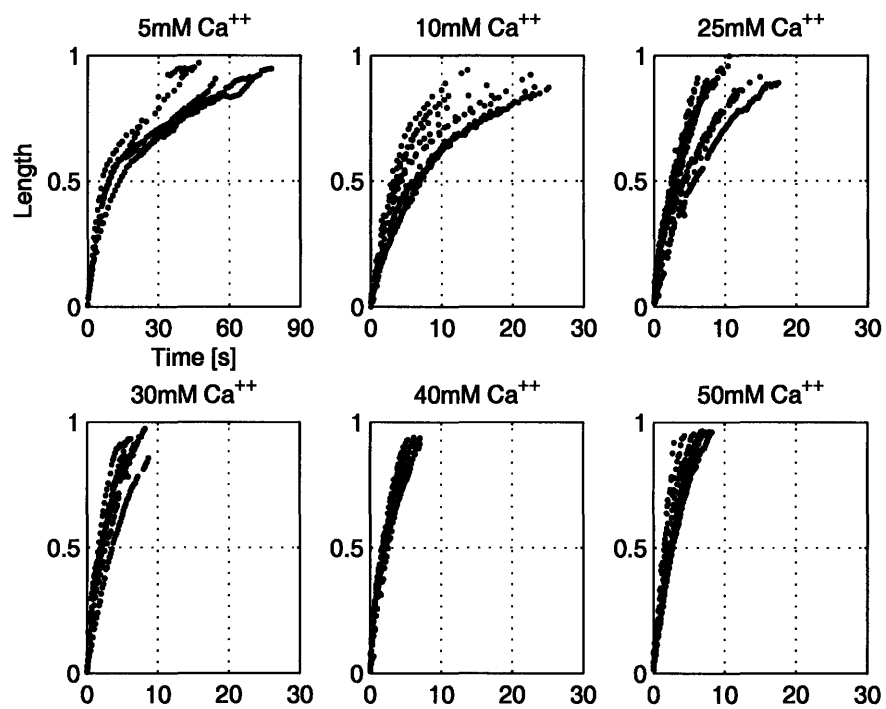
Figure 5-2: ormalized Length of Extension. A series of calcium titration experiments measuring the TD extension. Significant non-linear behavior is observed at all concentrations, though the total time of reaction decreases.

localized mechanism generates motion.

We can elaborate further on the implication that motion is generated via a localized mechanism by analyzing the calcium titration experiments. When the reaction is considered in the variables of length and time, a significant nonlinear behavior is observed. A simple explanation could involve viscous drag of the surrounding fluid opposing the extension and hence, slowing it down. To see why this cannot be so, we calculate the maximum viscous drag introduced by a fluid with a viscosity of 0.0015 Pa·s. The equation for drag due to a viscous liquid is

$$F_V \sim \frac{2\pi\mu_m x v}{\ln(\frac{x}{2R_a}) - 0.2}. \tag{5.1}$$

Using characteristic values for the viscosity of the fluid, radius, length, and velocity of the extending bundle, we find that the maximum viscous force exerted onto the bundle is $\sim$1 pN. From our experiments in the previous chapter, however, we know that the force generated in the extending acrosome is $\sim$2 nN, over a 1000 times greater than the opposing viscous force. Thus, a viscous opposing force cannot explain the deceleration observed in the extension.

Instead, we must consider the exact geometry of the bundle. To do so, we transform the length variable into volume with the equation

$$V = \int_0^L \pi r^2 \, dl. \tag{5.2}$$

Because the bundle is tapered and retains the shape of a truncated cone, the radius can be expressed as a function of the length l, giving $r=cl+r_0$. The total length Integrating over the entire length of the bundle, we find the relationship for the volume of a tapered rod as a function of length

$$V = \pi \left(c^2 \frac{L^3}{3} + c r_0 L^2 + r_0^2 L \right). \tag{5.3}$$

From [11], we know that $c = 7.3 \times 10^{-4}$ and $r_0 = 24$ nm.

With this relation in hand, we can recast the extension data in terms of the volume

70
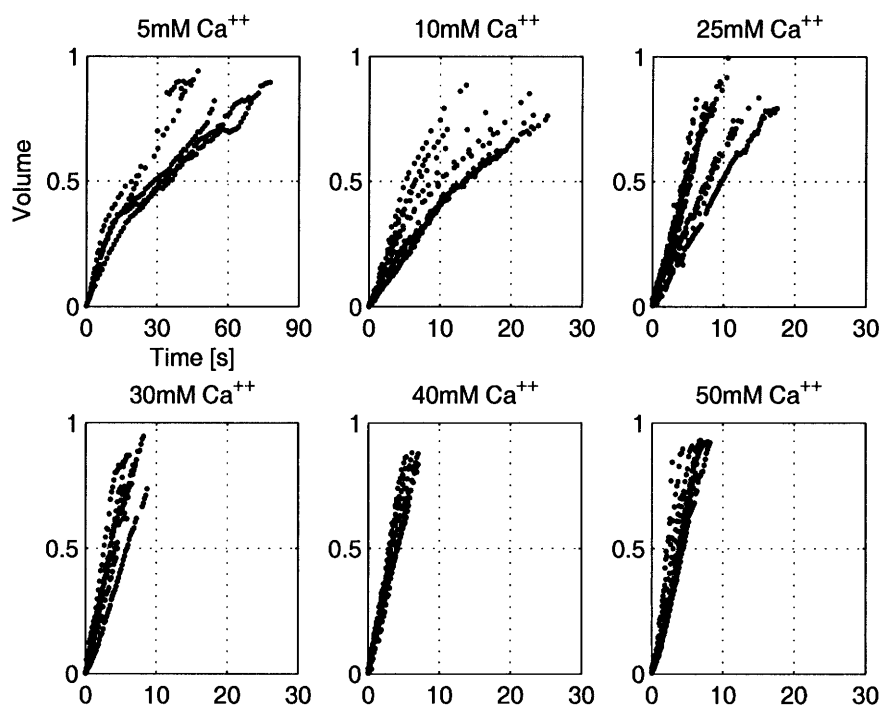
Figure 5-3: Normalized Volume of Extension. The nonlinearity is significantly removed when the exact volume of the bundle is accounted for. The nonlinearity and high variance for the low calcium (5, 10mM) data suggest stochastic binding behavior during Ca^{++}-CaM reaction.

extended as a function of time (Figure 5-3). We find that the predominant behavior of the extension is linear in time.

Moreover, the rate of this volume extension is dependent on the external calcium concentration. These two observations can be understood via a simple constant rate reaction Ca^{++}-CaM binding mechanism.

We represent this binding mechanism schematically as

$$CaM + Ca^{++} \xrightarrow{k} CaM \cdot Ca^{++} \qquad (5.4)$$
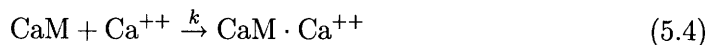
Here, k is an effective rate constant governing the conversion of the calcium-sensing scruin-CaM complex associated with the twisted bundle. Upon binding, this complex untwists the actin and extends the bundle, resulting in the observed TD extension,

71

CaM·Ca^{++}. Before we cast the above mechanism into mathematical form, we note that calcium concentration is essentially constant, since cellular dimensions are on the order of a few microns and diffusion of calcium ions occur on the order of milliseconds on this scale. Furthermore, the concentration of calmodulin participating in the reaction is constant and equal to the density of CaM in the bundle. This fixed amount of CaM participating in the reaction differs from the total concentration of CaM of the bundle. It is the time development of this latter quantity which we associate with the extension of the bundle, since this is the quantity conserved before and after the extension. With these assumptions, we let $x_0 = [Ca^{++}]$, $y = [CaM]$, and $z = [CaM·Ca^{++}]$ and write the rate equations for the above mechanism as

$$\frac{dx_0}{dt} = 0; \quad \frac{dy}{dt} = -kx_0y_0; \quad \text{and} \quad \frac{dz}{dt} = -\frac{dy}{dt} \tag{5.5}$$

We are interested in z because of its natural correspondence to the volume of the extended bundle. To establish this correspondence, we relate the number of CaM·Ca^{++} produced via this reaction to the number implied by the extending volume. In the former case, the number of molecules is calculated by multiplying z by the entire bundle volume, V_{tot}. In the latter case, we obtain the number of CaM·Ca^{++} converted to extend a given volume by multiplying the extended volume, V, by n, the density of CaM for a complete bundle. From our knowledge of the minimum and maximum number of filaments within the 60-μm long bundle, and the number of CaM in a micron of filament, we calculate be $n \sim 4.5\text{x}10^3$ M. The total number of CaM·Ca^{++} in a given volume of the extended bundle will be nV. This quantity is thus equal to zV_{tot} .

We can now solve for V and relate the observed slope, or volume reaction rate, to the kinetics associated with the CaM-Ca^{++} reaction. We arrive at

$$\overline{V} = \frac{kx_0y_0t}{n} \tag{5.6}$$

where we have normalized V by V_{tot} to obtain $\overline{V}$. We identify kx_0y_0/n as the slope, and solve for the rate constant, k. Figure 5-4a reports the measured slope and rate
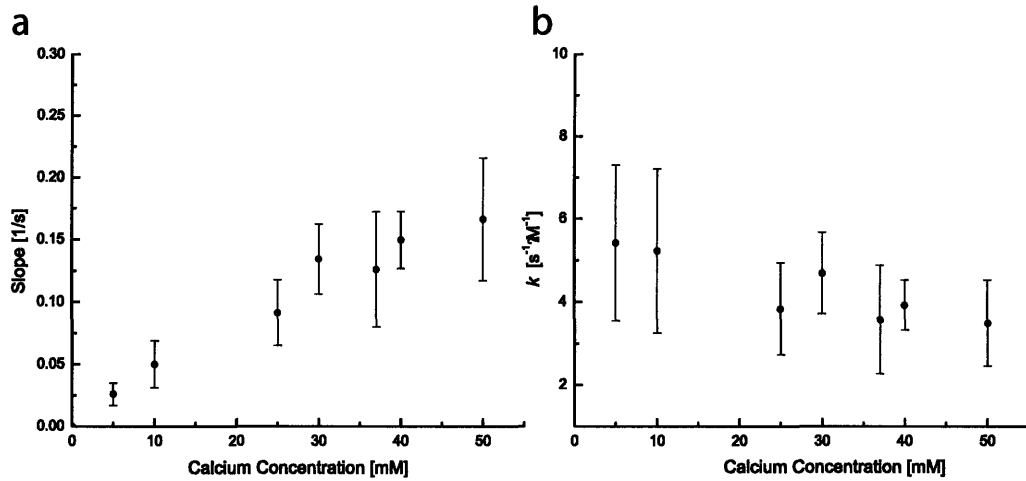
Figure 5-4: Binding Behavior. a. Rates were obtained by least-squares fitting of data in Figure 5-3. For 5 & 10mM calcium concentrations, only the initial linear regions were used to calculate the rate. b. Calculated rate constants using a non-cooperative, constant rate CaM-Ca++ binding mechanism. The slight dependence on [Ca++] suggests a deviation from the mechanism due to an over-estimation of [CaM] participating in the reaction.

constants as functions of x_0, the calcium concentration. We note that Figure 5-4a is consistent with our mechanism of a single Ca^{++} ion binding to CaM, as determined from the linear correlation between the slope and x_0. The values of k (Figure 5-4b) calculated are also reasonably consistent with binding constants observed for other calcium binding systems such as troponin [73]. We note that the order of magnitude for the rate constant is unity, but that the characteristic time for CaM conformational opening-closing is 10^4 s^{-1}. The drastic disparity suggests that our effective rate constant is convolved with an additional mechanism limiting the rate. Such a mechanism could be protein friction, as suggested and indeed, required by the theoretical model described in Chapter One [33, 34].

The mechanism proposed above invokes a single calcium-binding site on CaM. The reason for doing so is found in Figure 5-4, where we observe a near linear dependence of the volume reaction rate on calcium. This is indicative of one binding site. A bimolecular binding mechanism, i.e. 2 Ca^{++} binding to CaM, would imply a quadratic relationship between the slope and x_o, which we do not observe.
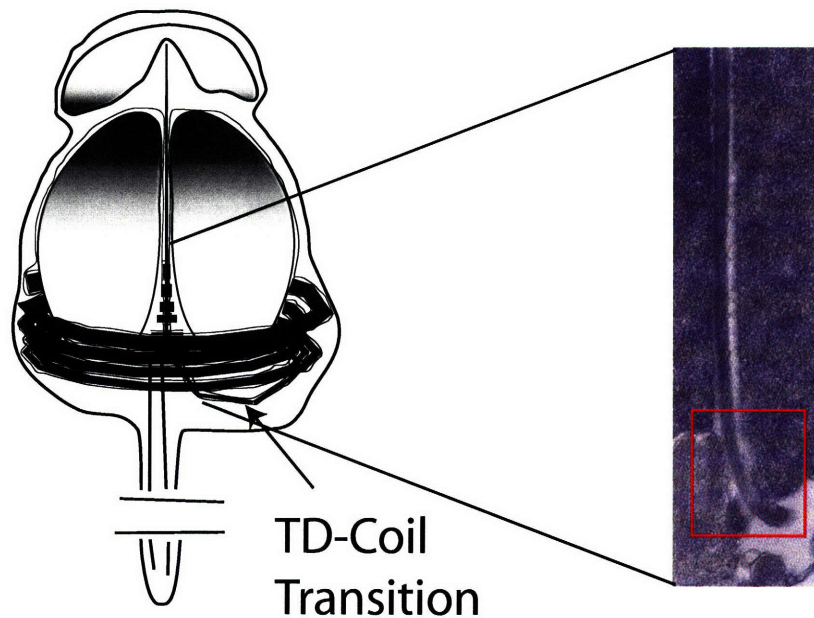
Figure 5-5: TD-Coil Transition Region. A representation of the TD-Coil transition region where calcium ions can bind, facilitating the TD reaction. The high curvature provide a preferential region for binding. The region also exhibits a non-zero twist gradient which constitutes the TD reaction.

Conclusion

The proposed mechanism also puts forth sequential binding and untwisting of CaM. Such a mechanism is consistent with the nature of the reaction because the Coil state transitions to the TD state at a discrete site. In addition, the high curvature associated with this TD-Coil interface bending into the nuclear channel presents a natural region for calcium ions to preferentially bind to CaM-a strain-induced lowering of the kinetics barrier would lead to higher binding affinity (Figure 5-5).

Knowledge of how calcium binds to calmodulin [23], and of the structural transformations of the actin bundle provides a physical basis with which to understand the acrosomal reaction [12]. This combination of functional, structural, and dynamical evidence reveals how mechanochemistry drives the actin spring, a primitive motile system which stores energy elastically and generates force to perform a crucial physiological function [31, 57].

In addition, this Coil-TD interface presents a natural region for calcium ions to bind to CaM because of the high curvature associated with the bundle bending into the nuclear channel. We believe this highly strained region allows significantly greater access to the Ca^{++} binding sites of CaM hence facilitating the reaction.

5.2   Calcium Delivery

The exact manner by which calcium ions enter the cell has not been previously investigated. Traditionally, a calcium ionophore has been used to induce the TD. This technique artificially delivers calcium ions into the cell, and is highly uncontrolled. Variations in the concentration, solubility, mixing, and transport of calcium-ionophore complexes complicate analysis of the actin spring system. Moreover, such a delivery technique bypasses any native mechanisms which may be present in the system.

To determine the existence and nature of native calcium transport mechanisms, we use laser induction. Recent experiments have suggested that calcium channels may be involved with the transport of calcium ions. Extensive literature exists documenting the numerous types and behavior of calcium channels [74]. Such channels exist in cells as diverse as neurons, glial cells, muscle cells, and gamete cells [75, 76, 77, 78]. Indeed, calcium channels have been found to participate in the acrosome reaction of sperm cells ranging from marine animals to mammals [79, 80, 81]. We use fluorescence microscopy to determine whether or not calcium channels exist on *Limulus* sperm cells.

Methods & Materials

100 μL of sperm cells were collected and washed in 500μL ASW. We prepared a 1:1000 dilution of the dye BODIPY-Verapamil (Invitrogen, Oregon, USA) in ASW. To this, we added 10 μL of cells and mixed gently. We incubated the cells at room temperature for 30 min isolated from light. We then spin the solution down for 2min at $\sim$600g, remove the supernatant and resuspend in 1mL ASW, and repeat the procedure to remove any excess dye. We use a TE-300 Nikon Epifluorescent Inverted

Microscope with a TR-X filter set to visualize the dye.

Results & Discussion

We use a BODIPY-conjugated calcium channel inhibitor, verapamil, to determine the existence of calcium channels on *Limulus* sperm. Verapamil binds to L-type voltage-gated calcium channels. Such channels are blocked by phenylalkylamines, of which verapamil is one. It is believed that verapamil binds within the ion-conducting mouth of the channel [82].

Cells were successfully labeled with the verapamil fluorescent dye (Figure 5-6). The dye did not bind to the cell membrane uniformly. Instead, two regions demonstrated preferred binding of the dye. The first region is near the acrosomal vesicle. Finding calcium channels at such a location suggests that calcium enters from the top of the cell body after initiation of the acrosome reaction. The vesicle bursts and calcium can enter the cell through the channels to take part in the extension. The second region is at the base of the cell, also suggestive of calcium entry during the reaction. Because the acrosome reaction requires a continuous supply of calcium to extend, the locations of calcium channels is consistent with their function.

a   b   c
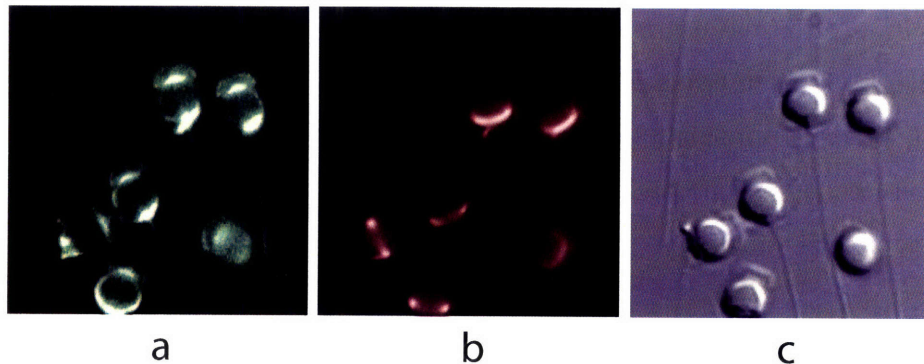
Figure 5-6: BODIPY-Verapamil & TR-Phalloidin Labelling. Fixed and labeled *Limulus* sperm cells. a. BODIPY-Verapamil labeling reveals a prominent number of L-type calcium channels near the base of the cell as well as within the acrosomal vesicle. b. Texas-Red Phalloidin labels the actin bundle. c. DIC image.

The presence of calcium channels also provides a possible explanation for how laser induction initiates the acrosome reaction. L-type channels are known to depend on

membrane depolarization/polarization for activation/deactivation. A localized event such as laser irradiation on the membrane may depolarize the membrane, leading to activation of the calcium channels.

Chapter 6

Conclusions & Outstanding Questions

Motion is a signature property of living systems. In *Limulus* sperm cells, dramatic motion of two forms is produced by an active actin spring. Our investigations into this system have revealed several important features which are fundamental to understanding the motions of the TD and FD. We have identified osmotic pressure as a method to induce the helical extension and retraction of the actin spring. Using this driving force, we have determined the work done during the extension. We compare this value with that of the elastic energy stored in the helical conformation and find that they are similar to $\sim 10^{-17}$ J.

We succeed in applying load forces on both the TD and FD reactions. Cells are embedded in agarose gels which impose frictional drag forces on the spring, thus stalling motion. By doing so, we find the maximum forces that the actin spring can generate. For the TD, we find a maximum stall force of ~ 2 nN. A value of ~ 8 nN was found for the FD. The disparity between these values suggest that force generation is a product of local conformation changes of the actin bundle, and hence scales with the cross-section of the bundle.

A sequential mechanism governing the TD reaction is further supported by a set of experiments involving calcium. We arrest the TD reaction by eliminating all calcium from the external environment as the spring extends. We show that re-introducing

calcium allows the reaction to begin again, thus showing behavior consistent with a sequential basis for the generation of motion. Further experiments using a titration series of calcium solutions are understood via a rate mechanism invoking a constant sequential binding of calcium to the identified calcium-sensitive protein calmodulin.

Our results confirm several assumptions built into the theoretical model governing the global dynamics of the actin spring. We have shown that the two local minima of the double well potential representing the coil and FD states are indeed similar in depths, and that the TD state is a global minimum. Our calcium experiments also are consistent with the central feature of the model, namely that the TD extension is a result of a sequential binding and untwisting of the actin bundle.

Though we have made significant progress in understanding the behavior of the actin spring, several key questions remain. Our calcium-CaM binding scheme details the kinetics of the reaction, but does not offer a mechanistic view of how such binding is rectified into the extension. A deeper explanation about force generation on a macromolecular scale is required. Such an explanation would involve knowledge of how local conformation changes of scruin give rise to the extension of the TD. Furthermore, the detailed structure of scruin still has yet to be determined.

Because actin is found in such a multitude of cellular systems, our work here suggests that energy stored and force generation based on twist may occur in those systems as well.

Bibliography

[1] J.V. Small, T. Stradal, E. Vignal, and K. Rottner. The lamellipodium: where motility begins. *Trends in Cell Biol.*, 12(3):112–120, 2002.

[2] I. Crevel, N. Carter, M. Schliwa, and R. Cross. Coupled chemical and mechanical reaction steps in a processive Neurospora kinesin. *The EMBO Journal*, 18:5863–5872, 1999.

[3] S. Inoue and E.D. Salmon. Force generation by microtubule assembly/disassembly in mitosis and related movements. *Mol. Biol. Cell*, 6(12):1619–40, 1995.

[4] K.C. Holmes. The swinging lever-arm hypothesis of muscle contraction. *Curr. Biol*, 7:R112–R118, 1997.

[5] V.C. Abraham, V. Krishnamurthi, D.L. Taylor, and F. Lanni. The Actin-Based Nanomachine at the Leading Edge of Migrating Cells. *Biophys. J.*, 77(3):1721–1732, 1999.

[6] J.T. Finer, R.M. Simmons, and J.A. Spudich. Single myosin molecule mechanics: piconewton forces and nanometre steps. *Nature*, 368:113–119, 1994.

[7] L.G. Tilney. Actin filaments in the acrosomal reaction of Limulus sperm. *J. Cell Biol.*, 64:289–310, 1975.

[8] L.G. Tilney, J.G. Clain, and M.S. Tilney. Membrane Events in the Acrosomal Reaction of Limulus Sperm: Membrane Fusion, Filament-Membrane Particle

Attachment, and the Source and Formation of New Membrane Surface. *J. Cell Biol.*, 81(1):229–253, 1979.

[9] G.G. Brown and W.J. Humphreys. Sperm-Egg interactions of *Limulus polyphemus* with scanning electron microscopy. *J. Cell Biol.*, 51(3):904–907, 1971.

[10] D.J. DeRosier, L.G. Tilney, E.M. Bonder, and P. Frankl. A change in twist of actin provides the force for the extension of the acrosomal process in limulus sperm: the false-discharge reaction. *J. Cell Biol.*, 93(2):324–337, 1982.

[11] J.H. Shin, L. Mahadevan, P.T. So, and P. Matsudaira. Bending stiffness of a crystalline actin bundle. *J. Mol. Biol*, 337:255–261, 2004.

[12] M.F. Schmid, M.B. Sherman, and P. Matsudaira. Structure of the acrosomal bundle. *Nature*, 431:104–107, 2004.

[13] L.G. Tilney, E.M. Bonder, and D.J. DeRosier. Actin filaments elongate from their membrane-associated ends. *J. Cell Biol.*, 90(2):485–494, 1981.

[14] M.B. Sherman, J. Jakana, S. Sun, P. Matsudaira, W. Chiu, and M.F. Schmid. The Three-dimensional Structure of the Limulus Acrosomal Process: A Dynamic Actin Bundle. *J. Mol. Biol.*, 294(1):139–149, 1999.

[15] J.H. Shin, M.L. Gardel, L. Mahadevan, P. Matsudaira, and D.A. Weitz. Relating microstructure to rheology of a bundled and cross-linked F-actin network in vitro. *Proc. Nat. Acad. Sci.*, 101(26):9636–9641, 2004.

[16] C. Owen and D. DeRosier. A 13-Å Map of the Actin-Scruin Filament from the Limulus Acrosomal Process. *J. Cell Biol.*, 123(2):337–344, 1993.

[17] M. Way, M. Sanders, C. Garcia, J. Sakai, and P. Matsudaira. Sequence and Domain Organization of Scruin, an Actin-Cross-Linking Protein in the Acrosomal Process of Limulus Sperm. *J. Cell Biol.*, 128:51–60, 1995.

[18] M.C. Sanders, M. Way, J. Sakai, and P. Matsudaira. Characterization of the Actin Cross-linking Properties of the Scruin-Calmodulin Complex from the Acrosomal Process of Limulus Sperm. *J. Biol. Chem.*, 271(5):2651, 1996.

[19] K.C. Holmes, D. Popp, W. Gebhard, and W. Kabsch. Atomic model of the actin filament. *Nature*, 347:44–49, 1990.

[20] C.J. Chapman, A.K. Puri, R.W. Taylor, and D.R. Pfeiffer. Equilibria between ionophore A23187 and divalent cations: stability of 1: 1 complexes in solutions of 80% methanol/water. *Biochemistry*, 26(16):5009–5018, 1987.

[21] W.L. Erdahl, C.J. Chapman, R.W. Taylor, and D.R. Pfeiffer. Ca2+ transport properties of ionophores A23187, ionomycin, and 4-BrA23187 in a well defined model system. *Biophys. J.*, 66(5):1678–1693, 1994.

[22] D. DeRosier, L. Tilney, and P. Flicker. A change in the twist of the actin-containing filaments occurs during the extension of the acrosomal process in *Limulus* sperm. *J. Mol. Biol.*, 137(4):375–89, 1980.

[23] D. Chin and A.R. Means. Calmodulin: a prototypical calcium sensor. *Trends in Cell Biol.*, 10:323, 2000.

[24] Y.S. Babu, C.E. Bugg, and W.J. Cook. Structure of calmodulin refined at 2.2 A resolution. *J. Mol. Biol.*, 204(1):191–204, 1988.

[25] J.L. Moreland, A. Gramada, O.V. Buzko, Q. Zhang, and P.E. Bourne. The Molecular Biology Toolkit (MBT): a modular platform for developing molecular visualization applications. *BMC Bioinformatics*, 2006.

[26] S. Linse, A. Helmersson, and S. Forsen. Calcium binding to calmodulin and its globular domains. *J. Biol. Chem.*, 266(13):8050–8054, 1991.

[27] B.A. Seaton, J.F. Head, D.M. Engelman, and F.M. Richards. Calcium-induced increase in the radius of gyration and maximum dimension of calmodulin measured by small-angle x-ray scattering. *Biochemistry*, 24:6740–6743, 1985.

[28] M.R. Nelson and W.J. Chazin. An interaction-based analysis of calcium-induced conformational changes in Ca^{2+} sensor proteins. *Prot. Sci.*, 7(2):270, 1998.

[29] M. Zhang, T. Tanaka, and M. Ikura. Calcium-induced conformational transition revealed by the solution structure of apo calmodulin. *Nature Struct. Biol.*, 2(9):758–767, 1995.

[30] A. Crivici and M. Ikura. Molecular and Structural Basis of Target Recognition by Calmodulin. *Ann. Rev. Biophys. Biomol. Struct.*, 24(1):85–116, 1995.

[31] J.H. Shin, L. Mahadevan, G.S. Waller, K. Langsetmo, and P. Matsudaira. Stored elastic energy powers the 60-μm extension of the Limulus polyphemus sperm actin bundle. *J. Cell Biol.*, 162(7):1183–1188, 2003.

[32] H. Kojima, A. Ishijima, and T. Yanagida. Direct Measurement of Stiffness of Single Actin Filaments with and Without Tropomyosin by *in vitro* Nanomanipulation. *Proc. of the Nat. Acad. of Sci.*, 91(26):12962–12966, 1994.

[33] L. Mahadevan, C.S. Riera, and J. Shin. Structural dynamics of an active actin spring. 2007.

[34] K. Tawada and K. Sekimoto. Protein friction exerted by motor enzymes through a weak-binding interaction. *J. Theor. Biol.*, 150(2):193–200, 1991.

[35] J. Howards. *Mechanics of Motor Proteins and the Cytoskeleton*. Sinauer Associates, Inc., 2001.

[36] J.M. Gere and S.P. Timoshenko. *Mechanics of Materials*. PWS-Kent Publishing Company, 1990.

[37] A.J. Hunt, F. Gittes, and J. Howard. The force exerted by a single kinesin molecule against a viscous load. *Biophys. J.*, 67(2):766–781, 1994.

[38] J.D. Ferry. *Viscoelastic Properties of Polymers*. John Wiley and Sons, 1980.

[39] F. Gittes, B. Schnurr, P.D. Olmsted, F.C. MacKintosh, and C.F. Schmidt. Microscopic Viscoelasticity: Shear Moduli of Soft Materials Determined from Thermal Fluctuations. *Phys. Rev. Lett.*, 79(17):3286–3289, 1997.

[40] A.J. Levine and TC Lubensky. One-and Two-Particle Microrheology. *Phys. Rev. Lett.*, 85(8):1774–1777, 2000.

[41] J.C. Crocker, MT Valentine, E.R. Weeks, T. Gisler, PD Kaplan, AG Yodh, and DA Weitz. Two-Point Microrheology of Inhomogeneous Soft Materials. *Phys. Rev. Lett.*, 85(4):888–891, 2000.

[42] T.G. Mason and D.A. Weitz. Optical Measurements of Frequency-Dependent Linear Viscoelastic Moduli of Complex Fluids. *Phys. Rev. Lett.*, 74(7):1250–1253, 1995.

[43] T.G. Mason. Estimating the viscoelastic moduli of complex fluids using the generalized Stokes-Einstein equation. *Rheol. Acta*, 39(4):371–378, 2000.

[44] P.M. Chaikin and T.C. Lubensky. *Principles of Condensed Matter Physics*. Cambridge University Press, 2000.

[45] W.P. Cox and E.H. Merz. Correlation of dynamic and steady viscosities. *J. Polym. Sci*, 28:619–622, 1958.

[46] J.L. McGrath, N.J. Eungdamrong, C.I. Fisher, F. Peng, L. Mahadevan, T.J. Mitchison, and S.C. Kuo. The Force-Velocity Relationship for the Actin-Based Motility of Listeria monocytogenes. *Current Biology*, 13(4):329–332, 2003.

[47] A. Goodman, Y. Tseng, and D. Wirtz. Effect of length, topology, and concentration on the microviscosity and microheterogeneity of DNA solutions. *J. Mol. Biol*, 323:199–215, 2002.

[48] M.L. Gardel, M.T. Valentine, J.C. Crocker, A.R. Bausch, and D.A. Weitz. Microrheology of Entangled F-Actin Solutions. *Phys. Rev. Lett.*, 91(15):158302, 2003.

[49] S. Wiesner, E. Helfer, D. Didry, G. Ducouret, F. Lafuma, M.F. Carlier, and D. Pantaloni. A biomimetic motility assay provides insight into the mechanism of actin-based motility. *J. Cell Biol.*, 160(3):387–398, 2003.

[50] H.C. Berg and L. Turner. Movement of microorganisms in viscous environments. *Nature*, 278:349–351, 1979.

[51] J.C. Crocker and D.G. Grier. Methods of digital video microscopy for colloidal studies. *J. Coll. Inter. Sci*, 179(1):298–310, 1996.

[52] M.J. Lang, C.L. Asbury, J.W. Shaevitz, and S.M. Block. An Automated Two-Dimensional Optical Force Clamp for Single Molecule Studies. *Biophys. J.*, 83(1):491–501, 2002.

[53] F. Gittes and C.F. Schmidt. Interference model for back-focal-plane displacement detection in optical tweezers. *Opt. Lett*, 23(1):7–9, 1998.

[54] K. Svoboda and S.M. Block. Biological applications of optical forces. *Ann. Rev. Biophys. Biomol. Struct.*, 23:247–85, 1994.

[55] K. Kamide. *Cellulose and Cellulose Derivatives: Molecular Characterization and Its Applications.* Elsevier, 2005.

[56] G. Ianniruberto and G. Marrucci. On compatibility of the Cox-Merz rule with the model of Doi and Edwards. *J. Non-Newt. Fl. Mech.*, 65(2):241–246, 1996.

[57] J.H. Shin, B.K. Tam, R.R. Brau, M.J. Lang, L. Mahadevan, and P. Matsudaira. Force of an actin spring. *Biophys. J.*, 92(10):1–5, 2007.

[58] T.D. Pollard. Assembly and dynamics of the actin filament system in nonmuscle cells. *J. Cell. Biochem.*, 31(2):87–95, 1986.

[59] H.M. Warrick and J.A. Spudich. Myosin Structure and Function in Cell Motility. *Ann. Rev. Cell Biol.*, 3(1):379–421, 1987.

[60] L. Mahadevan and P. Matsudaira. Motility Powered by Supramolecular Springs and Ratchets. *Science*, 288:95, 2000.

[61] M. Dogterom and B. Yurke. Measurement of the Force-Velocity Relation for Growing Microtubules. *Science*, 278:856, 1997.

[62] W.A. Linke, V.I. Popov, and G.H. Pollack. Passive and active tension in single cardiac myofibrils. *Biophys. J.*, 67(2):782–792, 1994.

[63] A. Ponti, M. Machacek, S.L. Gupton, C.M. Waterman-Storer, and G. Danuser. Two distinct actin networks drive the protrusion of migrating cells. *Science*, 305:1782–6, 2004.

[64] Y. Marcy, J. Prost, M.F. Carlier, and C. Sykes. Forces generated during actin-based propulsion: A direct measurement by micromanipulation. *Proc. Nat. Acad. Sci.*, 101(16):5992–5997, 2004.

[65] N. Kusukawa, M.V. Ostrovsky, and Mark M. Garner. Effect of gelation conditions on the gel structure and resolving power of agarose-based DNA sequencing gels. *Electrophoresis*, 20:1455–1461, 1999.

[66] N. Fatin-Rouge, K. Starchev, and J. Buffle. Size Effects on Diffusion Processes within Agarose Gels. *Biophys. J.*, 86:2710–2719, 2004.

[67] M.M. Tirado and J.G. de la Torre. Translational friction coefficients of rigid, symmetric top macromolecules. Application to circular cylinders. *J. Chem. Physics*, 71:2581, 1979.

[68] C.S. Farah and F.C. Reinach. The troponin complex and regulation of muscle contraction. *The FASEB Journal*, 9(9):755–767, 1995.

[69] J.L. Salisbury. Centrosomes: Sfi1p and Centrin Unravel a Structural Riddle. *Current Biology*, 14(1):27–29, 2004.

[70] K. Katoh and M. Kikuyama. An all-or-nothing rise in cytosolic [Ca^{++}] in *Vorticella sp*. *J. Exp. Biol.*, 200:35–40, 1997.

[71] W.J. Dong, C.K. Wang, A.M. Gordon, S.S. Rosenfeld, and H.C. Cheung. A Kinetic Model for the Binding of Ca2+ to the Regulatory Site of Troponin from Cardiac Muscle. *J. Biol. Chem.*, 272(31):19229–19235, 1997.

[72] J. Evenas, A. Malmendal, and M. Akke. Dynamics of the transition between open and closed conformations in a calmodulin C-terminal domain mutant. *Structure*, 9(3):185–95, 2001.

[73] W. Dong, S.S. Rosenfeld, C.K. Wang, A.M. Gordon, and H.C. Cheung. Kinetic studies of calcium binding to the regulatory site of troponin C from cardiac muscle. *J. Biol. Chem.*, 271(2):688–94, 1996.

[74] B. Hille. *Ion channels of excitable membranes.* Sinauer Sunderland, Mass, 2001.

[75] M.C. Nowycky, A.P. Fox, and R.W. Tsien. Three types of neuronal calcium channel with different calcium agonist sensitivity. *Nature*, 316(6027):440–443, 1985.

[76] B.P. Bean. Classes of Calcium Channels in Vertebrate Cells. *Annual Review of Physiology*, 51(1):367–384, 1989.

[77] TF McDonald, S. Pelzer, W. Trautwein, and DJ Pelzer. Regulation and modulation of calcium channels in cardiac, skeletal, and smooth muscle cells. *Physiol Rev*, 74(2):365–507, 1994.

[78] AE Lacerda, E. Perez-Reyes, X. Wei, A. Castellano, and AM Brown. T-type and N-type calcium channels of Xenopus oocytes: evidence for specific interactions with beta subunits. *Biophysical Journal*, 66(6):1833–1843, 1994.

[79] T. Kazazoglou, R.W. Schackmann, M. Fosset, and B.M. Shapiro. Calcium Channel Antagonists Inhibit the Acrosome Reaction and Bind to Plasma Membranes of Sea Urchin Sperm. *Proc. Nat. Acad. Sci.*, 82(5):1460–1464, 1985.

[80] A. Lievano. Ca^{++} Channels from the Sea Urchin Sperm Plasma Membrane. *J. Gen. Phys.*, 95, 1990.

[81] HM Florman. Sequential focal and global elevations of sperm intracellular Ca2+ are initiated by the zona pellucida during acrosomal exocytosis. *Dev Biol*, 165(1):152–64, 1994.

[82] G.H. Hockerman, B.D. Johnson, T. Scheuer, and W.A. Catterall. Molecular Determinants of High Affinity Phenylalkylamine Block of L-type Calcium Channels. *J. Biol. Chem.*, 270(38):22119, 1995.